공학박사 학위논문

Additive Manufacturing of Three-Dimensional Metal Nanostructure Arrays from Charged Aerosols

하전된 에어로졸을 이용한 삼차원 금속 나노구조물 어레이의 적층 제조

2020 년 2 월

서울대학교 대학원

기계항공공학부

정 우 익

Additive Manufacturing of Three-Dimensional Metal Nanostructure Arrays from Charged Aerosols

Wooik Jung
School of Mechanical and Aerospace Engineering
The Graduate School
Seoul National University

Abstract

Additive manufacturing, known as three-dimensional (3D) printing, aims to create any geometry over a large area in a fast, cost-effective manner. Although 3D-printed metal nanostructures are indispensable in many applications, reported 3D printing techniques for metals cannot achieve nanoscale resolution, fast speed, high purity, and intricate geometry simultaneously. Here, we introduce an aerosol 3D nanoprinting technique for manufacturing metal 3D nanostructure arrays in a parallel fashion at atmospheric pressure. Converging electric field lines caused by ion induced nanoscopic electrostatic lens guide charged aerosols to a precise location ensuring nanoscale resolution on a substrate with a programmed manner, and

it can therefore be treated as a drawing tool for 3D nanostructures. This technique exhibits two complementary modes: tip-directed growth and surface writing modes; the former enables printing various 3D nanostructures with flexibility including 3D nanopillar-like (e.g., vertical and overhanging nanopillars, helices) and 3D nanowall-like structures and the latter enables writing nanostructures following the repeated movement of nanostage such as ring and the letter "3D" structures. Unlike the existing 3D printing methods, the technique adopts a completely dry process that does not need any polymers or inks. The flexible choice of pure metals allows printing composite metal structures (e.g., Cu/Pd). High purity of nanoparticles within the structures enable sintering upon thermal treatment, thereby imparting enhanced mechanical strength (electrical conductivity shows only 6 times higher than bulk and elastic modulus has 10.5GPa). Further, we develop a phenomenological model to predict the resulting 3D geometry, which is consistent with the experimental results. The demonstrated capabilities foreshadow a new paradigm in nanofabrication.

Keywords: Additive manufacturing, Metal 3D printed metal nanostructure, Aerosol, Electric field lines, tip directed growth, surface writing

Student Number: 2013-23836

Contents

List of Tables

List of Figures

Chapter 1. Introduction

1.1. Research Background

Many 3D printing technologies developed today rely on different principles[1-8] and the flexibility and practicality of the resulting materials has enabled innovative products in electronics [1-3, 9, 10], energy devices [11, 12], robotics [13], bioengineering [14, 15], and sensing [16]. The success of 3D printing is mainly related to its ability to produce any desired geometry and architecture while adding novel functionalities. Additive manufacturing predominately focuses on the polymeric materials, but metals are indispensable owing to their many important functions [2-4, 17, 18]. In contrast with macroscopic 3D printing, downscaling to the nanoscale helps exploit the unique optical, physical, and chemical properties of micro/nanostructures [19, 20]. Existing 3D printing technologies, however, face serious challenges in ensuring nanoscale resolution while maintaining a high degree of freedom [1, 3, 4, 6, 7, 9]. In other words, no single printing technique can simultaneously provide high resolution, high purity, high printing speed, and intricate geometries.

Currently, diverse research activities aims to develop 3D metal nano printing at the micro- and submicrometer scale. Direct ink writing (DIW) [3, 21], Electrohydrodynamic printing (EHD) [2, 22], Laser assisted electrophoretic deposition [23, 24], Laser-induced forward transfer (LIFT) [25, 26], Meniscus-confined electroplating [1, 27], Electroplating of locally dispensed ions in

liquid[28], Laser-induced photoreduction [29] and Focused electron/ion beam induced deposition (FEBID/FIBID) [30, 31] techniques are already reported for the solution of 3D metal nanofabrication.

Despite all these efforts, there is no established solution in 3D metal nanoprinting field. In terms of feasible materials, current 3D printing of metals requires either photosensitive polymer metal mixture, or reducible metallic salts, or ideal rheological inks, thereby limiting the material choice [4, 17, 32]. From the view point of geometric flexibility, structures which have continuous body with angle over 90° relative to the z-axis are not reported. In addition, only a few researches are capable of parallel manufacturing process and require a lot of cost to implement them.

In this thesis, we introduce newly developed 3D metal nanoprinting strategy under atmospheric condition. This technique basically based on the previously developed ion-assisted aerosol lithography which can assemble charged nanoparticle with precise positioning in parallel fashion. This concept , however, only allows the creation of limited structures due to the prepatterns. To enabling high degree of freedom 3D metal nanoprinting, we suggest new methodology.

1.2. Research Objectives

This dissertation aims to develop a new methodology for the 3D metal nanoprinting from charged aerosols. To solve the limitation of reported 3D metal nanoprinting strategy, this technique shows material flexibility with high purity, unrestricted structure shape, large area, cost effective performance.

Owing to the previously developed nanoparticle assembly technique called ion assisted aerosol lithography, the basic concept for 3D metal nanoprinting was established [33-36]. However, only limited shapes are allowed in former lithography due to the prepatterns. Therefore, several strategy modifications were indispensable for complete 3D metal nanoprinting. We separate a dielectric mask with a hole array from a substrate, which is placed on a piozelectric nanostage.

Herein, we introduce a powerful 3D nano-printing technique for manufacturing metal nanostructure arrays. Diverse 3D metal nanostructures regulated by fine-tuning of the 3D translation of nanostage and their mechanical property data show versatile usefulness of our structure. Furthermore, theoretical studies support our nanoprinting strategy.

1.3. References

[1] Hu, J., Yu, M. F. Meniscus-confined three-dimensional electrodeposition for direct writing of wire bonds. *Science* **329**, 313–316 (2010).

[2] Park, J. U., Hardy, M., Kang, S. J., Barton, K., Adair, K., Mukhopadhyay, D. K., Lee, C. Y., Strano, M. S., Alleyne, A. G., Georgiadis, J. G., Ferreira, P. M., Rogers, J. A. High-resolution electrohydrodynamic jet printing. *Nat. Mater.* **6**, 782–789 (2007).

[3] Ahn, B. Y., Duoss, E. B., Motala, M. J., Guo, X., Park, S. I., Xiong, Y., Yoon, J., Nuzzo, R. G., Rogers, J. A., Lewis, J. A. Omnidirectional printing of flexible, stretchable, and spanning silver microelectrodes. *Science* **323**, 1590–1593 (2009).

[4] Oran, D., Rodriques, S. G., Gao, R. Asano, S., Skylar-Scott, M. A., Chen, F., Tillberg, P. W., Marblestone, A. H., Boyden, E. S. 3D nanofabrication by volumetric deposition and controlled shrinkage of patterned scaffolds. *Science* **362**, 1281–1285 (2018).

[5] Gao, H., Hu, Y., Xuan, Y., Li, J., Yang, Y., Martinez, R. V., Li, C., Luo, J. Qi, M., Cheng, G. J. Large-scale nanoshaping of ultrasmooth 3D crystalline metallic structures. *Science* **346**, 1352–1356 (2014).

[6] Kotz, F., Arnold, K., Bauer, W., Schild, D., Keller, N.,

Sachsenheimer, K., Nargang, T. M., Richter, C., Helmer, D., Rapp, B. E. Three-dimensional printing of transparent fused silica glass. *Nature* **544**, 337–339 (2017).

[7] Martin, J. H., Yahata, B. D., Hundley, J. M., Mayer, J. A., Schaedler, T. A., Pollock, T. M. 3D printing of high-strength aluminium alloys. *Nature* **549**, 365–369 (2017).

[8] Kelly, B. E., Bhattacharya, I., Heidari, H., Shusteff, M., Spadaccini, C. M., Taylor, H. K. Volumetric additive manufacturing via tomographic reconstruction. *Science* **363**, 1075–1079 (2019).

[9] Saleh, M. S., Hu, C. S., Panat, R. Three-dimensional microarchitected supple and devices using nanoparticle assembly by pointwise spatial printing. *Sci. Adv.* **3**, e1601986 (2017).

[10] Lewis, J. A., Ahn, B. Y. Device fabrication: Three-dimensional printed electronics. *Nature* **518**, 42–43 (2015).

[11] Wei, T. S., Ahn, B. Y., Grotto, J., Lewis, J. A. 3D printing of customized Li-ion batteries with thick electrodes. *Adv. Mater.* **30**, e1703027 (2018).

[12] Sun, K., Wei, T. S., Ahn, B.Y., Seo, J. Y., Dillon, S. J., Lewis, J. A. 3D printing of interdigitated Li-ion microbattery architectures. *Adv. Mater.* **25**, 4539–4543 (2013).

[13] Wehner, M., Truby, R. L., Fitzgerald, D. J., Mosadegh, B., Whitesides, G. M., Lewis, J. A., Wood, R. J. An integrated design

and fabrication strategy for entirely soft, autonomous robots. *Nature* **536**, 451–455 (2016).

[14] Dvir, T., Timko, B. P., Kohane, D. S., Langer, R. Nanotechnological strategies for engineering complex tissues. *Nat. Nanotechnol.* **6**, 13–22 (2011).

[15] Lutolf, M. P., Hubbell, J. A. Synthetic biomaterials as instructive extracellular microenvironments for morphogenesis in tissue engineering. *Nat. Biotechnol.* **23**, 47–55 (2005).

[16] Stewart, M. E., Anderton, C. R., Thompson, L. B., Maria, J., Gray, S. K., Rogers, J. A., Nuzzo, R. G. Nanostructured plasmonic sensors. *Chem. Rev.* **108**, 494–521 (2008).

[17] Vyatskikh, A., Delalande, S., Kudo, A., Zhang, X., Portela, C. M., Greer, J. R. Additive manufacturing of 3D nano-architected metals. *Nat. Commun.* **9**, 593 (2018).

[18] Gibson, M. A., Mykulowycz, N. M., Shim, J., Fontana, R., Schmitt, P., Roberts, A., Ketkaew, J., Shao, L., Chen, W., Bordeenithikasem, P., Myerberg, J. S., Fulop, R., Verminski, M. D., Sachs, E. M., Chiang, Y. M., Schuh, C. A., Hart, A. J., Schroers, J. 3D printing metals like thermoplastics: Fused filament fabrication of metallic glasses. *Mater. Today* **21**, 697–702 (2018).

[19] Ozbay, E. Plasmonics: Merging photonics and electronics at nanoscale dimensions. *Science* **311**, 189–193 (2006).

[20] Valiev, R. Materials science: nanomaterial advantage. *Nature* **419**, 887 (2002).

[21] Skylar-Scott, Mark A., Suman Gunasekaran, and Jennifer A. Lewis. "Laser-assisted direct ink writing of planar and 3D metal architectures." *Proceedings of the National Academy of Sciences* 113.22 (2016): 6137-6142.

[22] Galliker, Patrick, et al. "Direct printing of nanostructures by electrostatic autofocussing of ink nanodroplets." *Nature communications* 3 (2012): 890.

[23] Iwata, Futoshi, and Junya Metoki. "Microelectrophoresis deposition using a nanopipette for three-dimensional structures." *2014 International Conference on Manipulation, Manufacturing and Measurement on the Nanoscale (3M-NANO)*. IEEE, 2014.

[24] Zhao, Chenglong, Piyush J. Shah, and Luke J. Bissell. "Laser additive nano-manufacturing under ambient conditions." *Nanoscale* 11.35 (2019): 16187-16199.

[25] Zenou, Michael, Amir Sa'ar, and Zvi Kotler. "Laser transfer of metals and metal alloys for digital microfabrication of 3D objects." *Small* 11.33 (2015): 4082-4089.

[26] Visser, Claas Willem, et al. "Toward 3D printing of pure metals by laser-induced forward transfer." *Advanced materials* 27.27 (2015):

4087-4092.

[27] Seol, Seung Kwon, et al. "Electrodeposition-based 3D printing of metallic microarchitectures with controlled internal structures." *Small* 11.32 (2015): 3896-3902.

[28] Momotenko, Dmitry, et al. "Write–read 3D patterning with a dual-channel nanopipette." *ACS nano* 10.9 (2016): 8871-8878.

[29] Ishikawa, Atsushi, Takuo Tanaka, and Satoshi Kawata. "Improvement in the reduction of silver ions in aqueous solution using two-photon sensitive dye." *Applied physics letters* 89.11 (2006): 113102.

[30] Plank, Harald, et al. "The influence of beam defocus on volume growth rates for electron beam induced platinum deposition." *Nanotechnology* 19.48 (2008): 485302.

[31] Höflich, Katja, et al. "The Direct Writing of Plasmonic Gold Nanostructures by Electron-Beam-Induced Deposition." *Advanced materials* 23.22-23 (2011): 2657-2661.

[32] An, B. W., Kim, K., Lee, H., Kim, S. Y,. Shim, Y., Lee, D. Y., Song, J. Y., Park, J. U. High-resolution printing of 3D structures using an electrohydrodynamic inkjet with multiple functional inks. *Adv. Mater.* **27**, 4322–4328 (2015).

[33] Kim, H., Kim, J., Yang, H., Suh, J., Kim, T., Han, B., Kim, S., Kim, D. S., Pikhitsa, P. V., Choi, M. Parallel patterning of nanoparticles

via electrodynamic focusing of charged aerosols. *Nat. Nanotechnol.* **1**, 117–121 (2006).

[34] Lee, H., You, S., Woo, C. G., Lim, K., Jun, K., Choi, M. Focused patterning of nanoparticles by controlling electric field induced particle motion. *Appl. Phys. Lett.* **94**, 053104 (2009).

[35] You, S., Han, K., Kim, H., Lee, H., Woo, C. G., Jeong, C., Nam, W., Choi, M. High-resolution, parallel patterning of nanoparticles via an ion-induced focusing mask. *Small* **6**, 2146–2152 (2010).

[36] Lee, H., You, S., Pikhitsa, P. V., Kim, J., Kwon, S., Woo, C. G., Choi, M. Three-dimensional assembly of nanoparticles from charged aerosols. *Nano Lett.* **11**, 119–124 (2011).

Chapter 2.

Manufacturing 3D metal nanostructure via Ion Assisted Aerosol Lithography

2.1 Introduction

Ion assisted aerosol lithography (IAAL)[1-4] is an aerosol-based 3D assembly technique, which utilizes electrostatic focusing effects to manipulate the trajectory of incoming charged nanoparticles (Details of IAAL will be deal with next section). Charged aerosols can be directed into openings in photoresist patterns or apertures in masks, making it possible to produce 3D nanoparticle structures whose shapes are defined by the cross-section of the openings in the photoresist layer or the mask.

Building upon this, here we show that translating the mask during the nanoparticle deposition process holds promises to be a novel 3D nano-printing technique. The shapes of the 3D nanoparticle structures are now determined not only by the cross-section of the mask openings, but also by the mask trajectory. Interestingly, we found that varying the horizontal mask translation speed leads to two distinct process regimes: '3D growth' mode at slower translation speeds and '3D writing' mode at faster translation speeds.

In '3D growth' mode, high aspect ratio nanowires can be assembled by vertical upward translation of the mask during particle deposition. In principle, the process can continue indefinitely by matching the mask translation speed to the vertical growth rate of the structures. Adding horizontal components in the mask motion allows for creation of structures

with various 3D shapes, such as slanted pillars or helices. In ‘surface writing’ mode, faster horizontal translation of the mask causes the particles to land next to the existing clusters rather than being deposited on them. This enables particle assembly whereby the structures do not lift off vertically from the substrate. Multiple sweeps of a given trajectory while depositing particles allow the clusters to grow in thickness and become ‘walls’.

In addition to the presented capability of directly printing 3D shapes using this technique, the ability to switch the aerosol material on demand with relative ease contributes to the expected versatility of this process, and further development and fine tuning will benefit applications that require multi-material 3D nanostructures.

Furthermore, to practical use of versatile applications, investigation of mechanical property should be conducted. Owing to the fully dry process, the manufactured 3D nanostructures have rarely impurities and this leads to the outstanding mechanical robustness. The analysis of electrical conductivity and mechanical strength show high possibility to versatile applications for metal nanodevices.

2.2 Method

2.2.1 Nanoparticle generation and characteristics

We produce charged aerosols by spark ablation system. Spark ablation can simultaneously generate both ions and charged nanoparticles [5, 6]. Ions, together with the dielectric patterns on the mask, can reshape the electric field lines, whereas nanoparticles provide the building blocks for 3D nanoprinting. This method is based on an RLC electrical circuit assembled from a resistor, an inductor, and a capacitor. A current source—converted by a DC power supply at 6.5 kV (FuG Elektronik GmbH, HCP 140-12500) and a resistor of 20 MΩ—constantly charges the capacitor, which is connected in parallel to a pair of electrodes. The electrodes—a wire with a diameter of 1 mm and a cylinder with outer and inner diameters of 2 and 1.6 mm, respectively—were separated by a gap of approximately 1 mm, through which an inert gas (N_2, purity 99.999%) is continuously flowing. The flow rate was 2 lpm, and it controlled by a mass flow controller MKS 247D. When the voltage over the capacitor breaks down the gas between the electrodes, a spark discharge is formed. As a result, the vaporized electrode material condenses to form nanoparticles.

In this work, we used two pairs of electrodes: one made of palladium (Thermo Fisher, 1 mm diameter, 99.98% purity, 2 mm diameter, 99.95% purity) and the other made of copper (Thermo Fisher, 1 mm diameter, 99.999% purity, 2 mm diameter, 99.999% purity). We measured the size distribution of the nanoparticles using a scanning mobility particle sizer (SMPS), which consists of an aerosol neutralizer (TSI 3077), a differential mobility analyzer (TSI 3085), and a condensation particle counter (TSI 3776) as shown in Figure 2.1. The size distributions of Cu and Pd nanoparticles generated by spark discharge are shown in Figure 2.2.

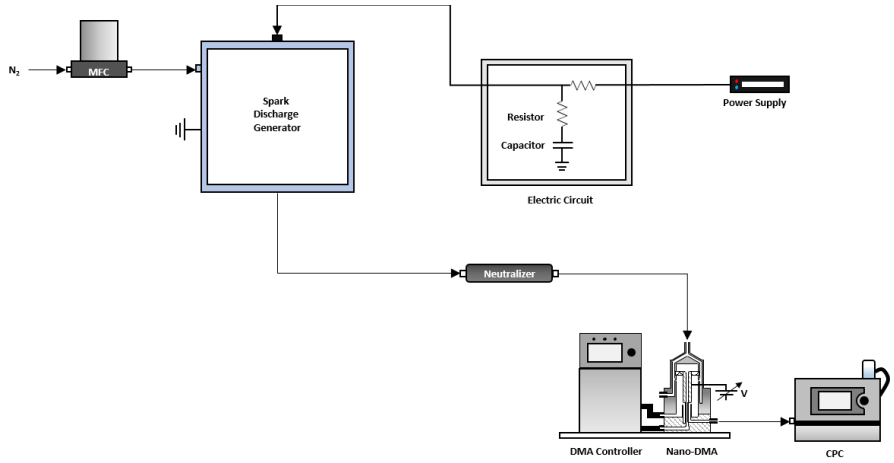

Figure 2.1. Schematic illustrations of spark ablation system and scanning mobility particle sizer (SMPS).

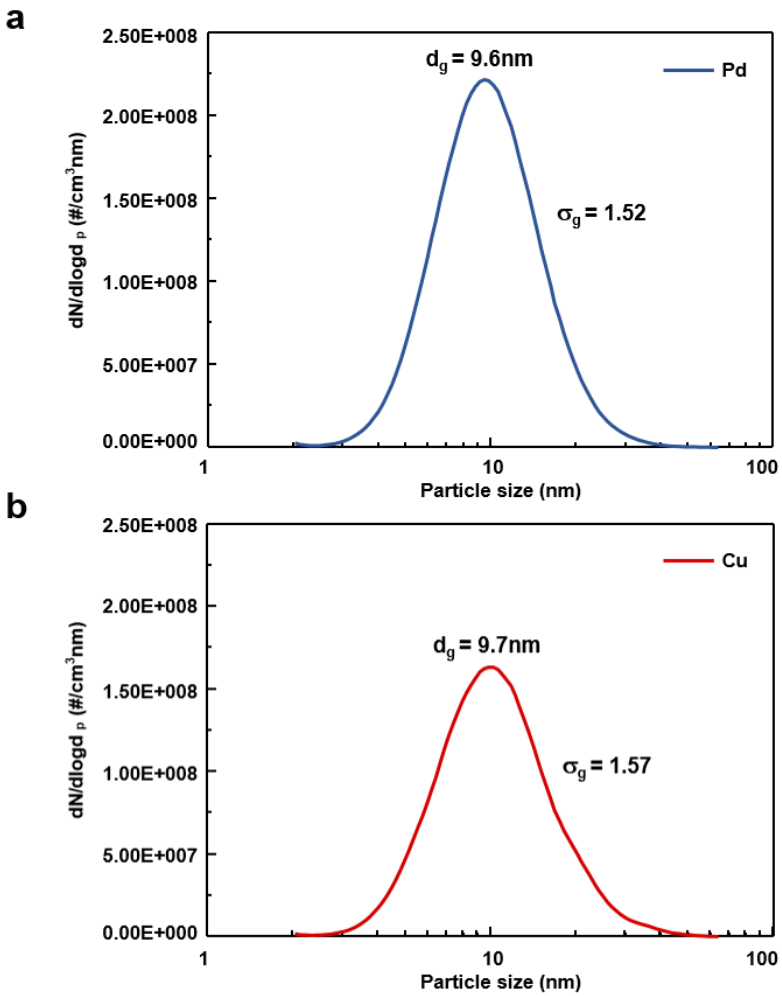

Figure 2.2. Size distribution of nanoparticles measured by the Scanning Mobility Particle Sizer (SMPS). Size distributions of (**a**) Pd and (**b**) Cu nanoparticles show a geometric mean diameter d_g = 9.6 nm for Pd and d_g = 9.7 nm for Cu and a geometric standard deviation of σ_g = 1.52 for Pd and σ_g = 1.57 for Cu. d_p is the *y*-axis means nanoparticle diameter.

2.2.2. Ion Assisted Aerosol Lithography

Ion assisted aerosol lithography (IAAL) is an aerosol-based 3D assembly technique, which utilizes electrostatic focusing effects to manipulate the trajectory of incoming charged nanoparticles. Charged aerosols can be directed into opening in photoresist patterns or apertures in masks, making it possible to produce 3D nanoparticle structures whose shapes are defined by the cross-section of the opening in the photoresist layer or the mask. Figure 2.3 presents ion assisted aerosol lithography [1-4].

Charged aerosols (ions and nanoparticles) which generated by spark ablation system are injected into a electrostatic precipitator (ESP) chamber and they are attracted to a substrate by opposite electrical potential. Ions have much faster mobility than nanoparticles, so reaching the substrate first and accumulated on the non-conductive photoresist patterns. Deposited ions convert electrical potential lines and they act as an electrostatic focusing lens. After then, charged nanoparticles are deposited on the opening site of substrate by following focused electric field line. Therefore, high resolution nanopatterns can be manufactured throughout the IAAL (cf. Figure 2.4).

As presented above, IAAL is a fancy aerosol-based technique which enables precise positioning of nanoparticles. This high resolution and parallel nanoparticle assembly technique can fabricate a variety of

nanostructures that can be applied toward gas sensor [7], solar cell [8] and surface enhanced raman spectroscopy (SERS) [9].

The manufactured nanostructures are much smaller than opening site of the original photoresist pattern. However, the shape of nanostructures are governed by a prepatterned substrate so it has a restriction.

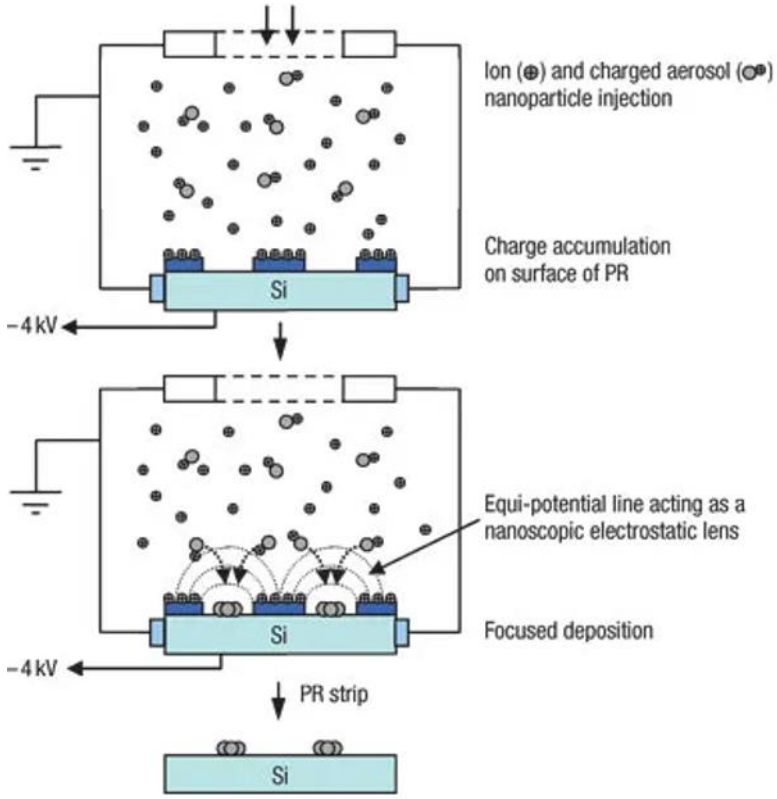

Figure 2.3. Schematic for ion assisted aerosol lithography [1].

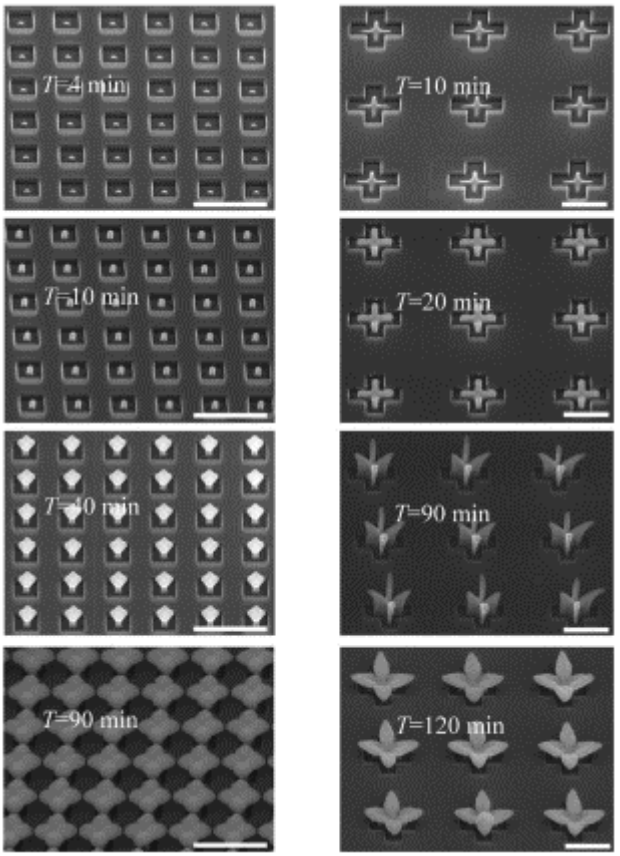

Figure 2.4. Time dependent growth of 3D nanoparticle structure arrays through ion assisted aersosol lithography [4].

2.2.3 Concept for 3D metal nanoprinting via ion assisted aerosol lithography

Previously, we developed an ion assisted aerosol lithography (IAAL), which can assemble aerosols to form an array of 3D nanostructures [1-4]. The system consisted of an aerosol particle source and a deposition chamber in which a silicone substrate patterned by a dielectric layer was placed under a given electric field. While the method constructed various 3D nanostructures for different applications by changing the shape of prepatterns, only limited geometries were allowed according to the prepatterns made on the substrate [7-9]. Subsequent removal of prepatterns was also required. Therefore, it is necessary to developing newly designed 3D nanoprinting methodology enabling the the metal nanostructures with the flexibility of geometry, feature size and material in a parallel fashion.

Herein, we introduce a 3D nanoprinting method based on aerosol technology for manufacturing 3D metal nanostructure arrays in a parallel fashion at atmospheric pressure without the use of any polymers or liquids. As shown in Figure 2.5, charged aerosols and ions are simultaneously injected through aerosol inlet into an electrostatic chamber where a dielectric mask having a hole array is separated from a Si substrate which is controlled by a piezoelectric nanostage. By applying a negative potential to the substrate, positively charged aerosols and positive ions are attracted towards the

floating mask and the substrate. High mobility positive ions first arrive at the surface of the floating mask prior to lower mobility charged aerosols in a given electric field. The accumulation of ions on the surface of the dielectric mask occurs and distorts originally flat equipotential lines into convex lines around each hole of the floating mask (see the inset of Figure 2.5b) and generates an invisible electrostatic lens around each hole since the electric field lines are in a perpendicular direction to the equi-potential lines. Therefore, charged aerosols are focused following the converging electric field lines. In this way, positively charged aerosols are guided through the hole in a converging manner without touching or depositing on the surface of the floating mask, which is positively charged by (positive) ion accumulation. This floating mask is similar to the nozzle concept used in other 3D printing techniques, but the width of printed 3D structures is much smaller than the hole size due to the above-mentioned focusing effect. While a focused narrow stream of charged aerosols deposits on a substrate, we program the 3D nanostage translation to control the geometry of the 3D nanostructures as shown in Figure 2.5b.

Produced aerosols and ions were carried into to the 3D printing system and first met a floating mask. A floating mask was made from a Si wafer coated with a layer of 1 μm thick Si3N4; the detailed dimensions are listed in Table 2.1 in the end of Chapter 2. The fabrication process required a few steps following reactive ion etching and wet etching processes (cf. Figure

2.6). The substrate was a highly doped p-type silicon (1 cm× 1 cm), and it was placed beneath the mask at an initial distance of a few micrometers (depending on the experiments). For maintaining a distance between the mask and the substrate, we installed three capacity sensors (Unipulse Corporation, PS-Ⅲ-3D) at an equidistance from the center of the mask. All experiments are conducted once the three capacity sensors indicate an identical distance (see Figure 2.7 for the floating mask and substrate leveling system). A negative potential of −1.5 kV was constantly applied to the substrate, which was attached to a nanostage (Thorlabs, MAX 313D/M). The surface potential distribution of the mask was measured to be 658 μV using a Kelvin force microscope (Park systems, NX10) (see data in Figure 2.8); SEM images were recorded using a Carl Zeiss SUPRA55VP with 2 kV electron beam, and at a tilted view (40°) SEM images were captured; and EDS data were collected by a Bruker FlatQUAD. For the phenomenological model, we used the mathCAD program for the calculations.

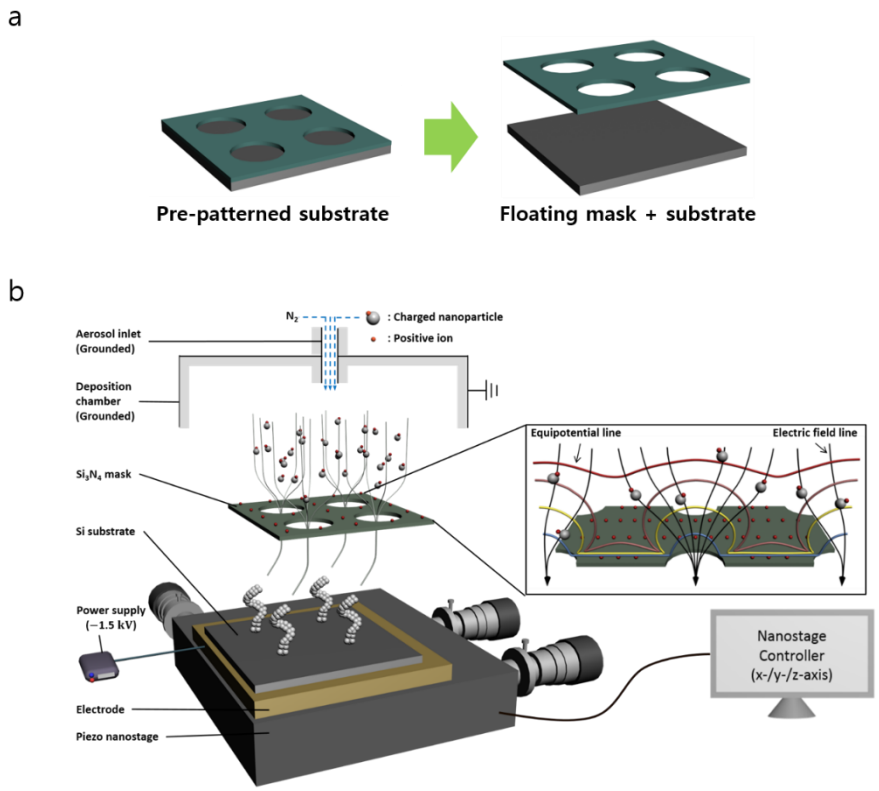

Figure 2.5. (a) Comparison between pre-patterned substrate and current status of floating mask with substrate. **(b)** Schematic of 3D nanoprinting setup, which consists of a nanoparticle source, floating mask, and piezoelectric nanostage. Here, the nanoparticles are supplied by spark ablation. Without using a charging device, this method produces a high fraction of charged particles and ions. A negative potential is applied to the substrate, which attracts both cations and positively charged nanoparticles. The ions with higher mobility arrive at the substrate beforehand. Some of them are deposited on the dielectric surface, while the rest pass through the

holes and are subsequently neutralized by the substrate. The former process generates nanoscopic electrostatic focusing lenses and converging electric field lines around each hole. Therefore, charged nanoparticles are focused following the converging electric field lines.

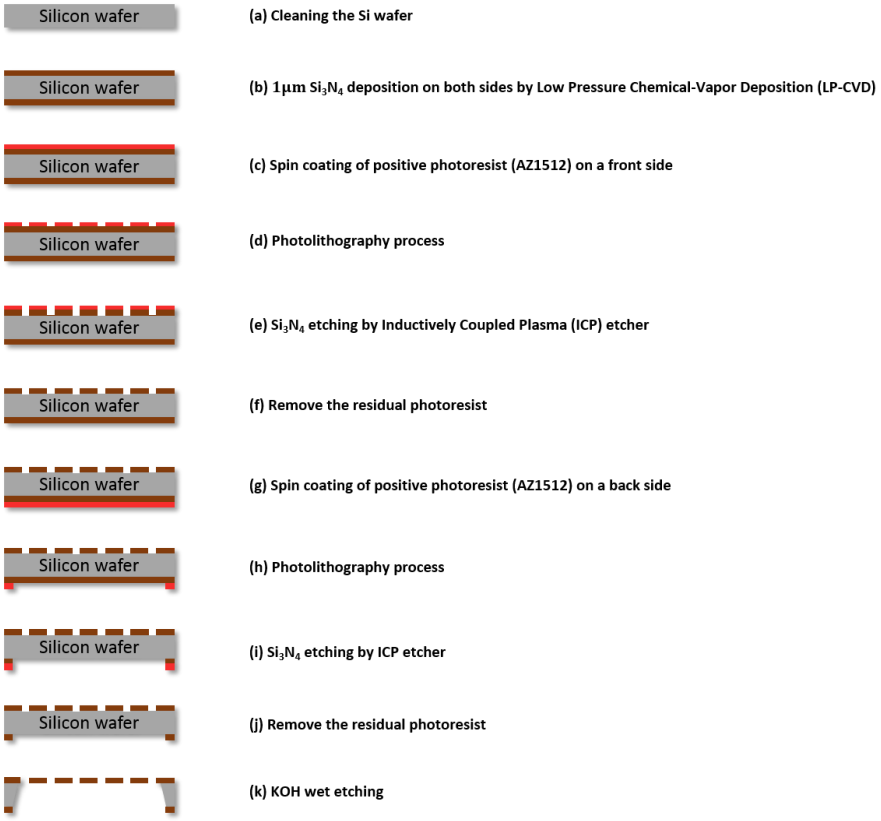

Figure 2.6. Fabrication process of the floating mask.

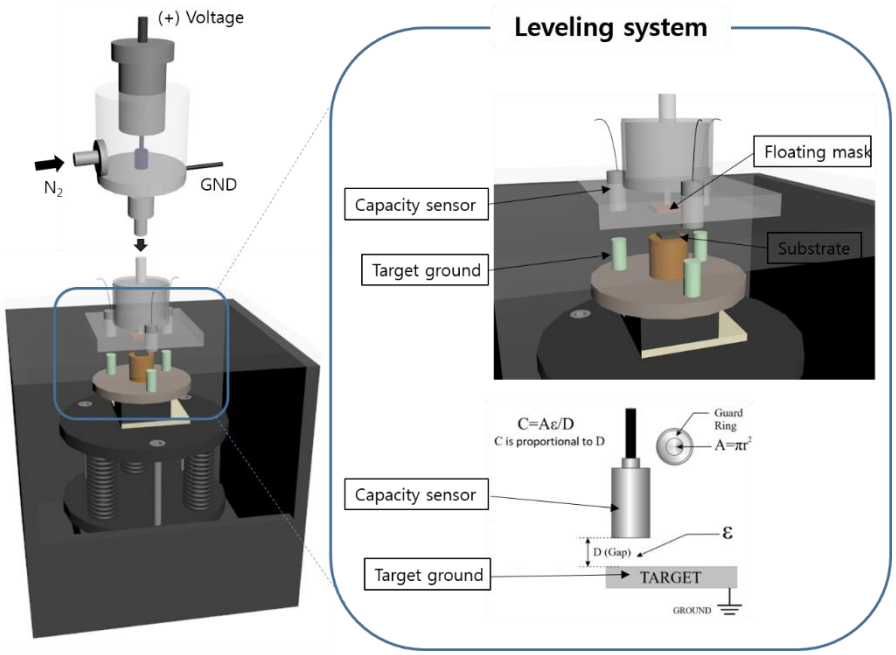

Figure 2.7. Schematic of floating mask and substrate leveling system. Three capacity sensors placed around floating mask align the distance between floating mask and substrate.

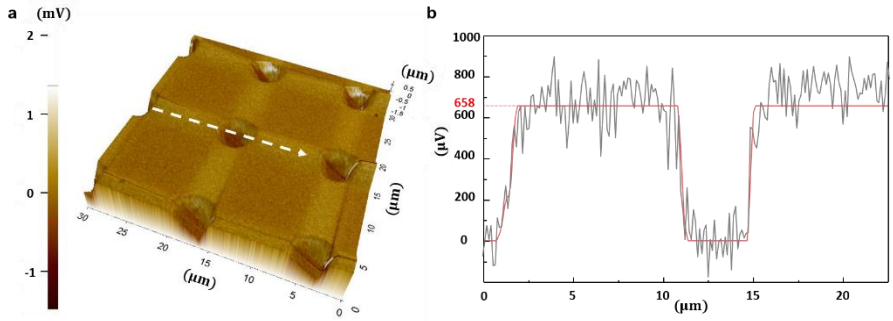

Figure 2.8. Surface potential distribution of the Si_3N_4 (**a**) 3D surface potential distribution of the mask. (**b**) Kelvin force microscope (KFM) data of the surface potential distribution confirm ion charge accumulation on the Si_3N_4 mask. The black line is the raw data, and the red line represents the average of these data (658 μV).

2.3 Result and Discussion

2.3.1 Tip-directed growth of 3D metal nanostructure

As mentioned above in Method chapter, reshaped electric field lines direct the charged nanoparticles, thus initiating 3D nanoprinting. Positive ions that accumulate on the dielectric mask repel the deposition of the nanoparticles with the same polarity over the mask but not from the holes in which much smaller virtual nozzles are generated due to the focusing. This therefore allows the printed 3D structures to have a width smaller than the hole size. Once the initial tips of the structures are developed, the charged nanoparticles are continuously deposited over the tips. Upon deposition, these tips are actually protruding elements of the conductive surface. Near the tip, electric field lines are strongly concentrated, thereby attracting the incoming nanoparticles. When the nanostage is kept still, all the pillars grow normal to the substrate while maintaining an identical height. A high aspect ratio of 36.7 (length: 11 μm, width: 0.3 μm) is achieved by prolonging the printing time meanwhile moving down the nanostage along the z-direction (cf. Figure 2.9, a to c). The diameter of the nanopillars is 0.3 μm, much smaller than the hole size (4 μm) on the mask. This drastic difference is due to the above mentioned sharply converged electric field lines around each

hole.. The density of the array structures on the substrate can be increased by horizontally shifting the nanostage in a sequence (cf. Figure 2.10 and SEM image of top view with the detailed steps of horizontal nanostage shift in Figure 2.10b). The material types of nanoparticles can be switched during deposition process, which enables printing composite nanopillars consisting of an upper part of Cu and a bottom Pd part (cf. Figure 2.11).

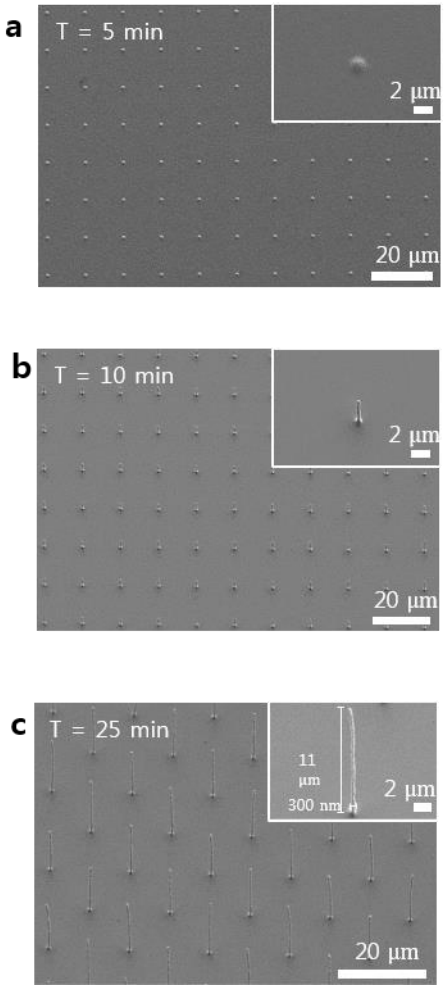

Figure 2.9. Pd nanopillar structures with different printing times. (a) 5 min, **(b)** 10 min, **(c)** 25 min. To fabricate pillars with a high aspect ratio **(**length: 11 μm, width: 0.3 μm) **(c),** the nanostage holds still for 10 min and then translates along the z-axis at 10 $\mathrm{nm\,s^{-1}}$. The inset pictures are tilted view.

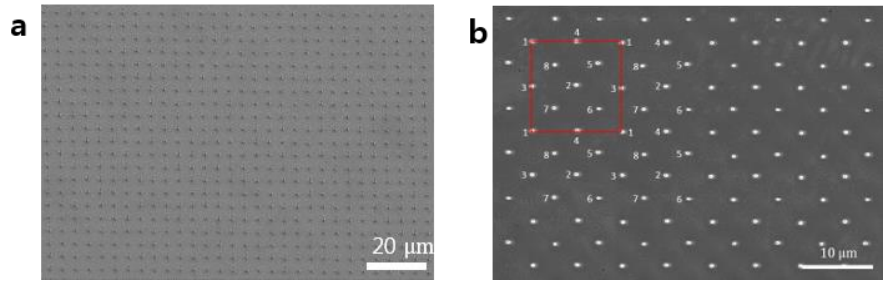

Figure 2.10. Horizontal stage movement for increase array density. Pd nanopillars array with increased density from 236 structures to 770 structures on a surface area of 100 × 100 μm^2, which was realized by moving the stage horizontally in a sequential manner. In particular, we programmed the nanostage to move in eight steps, each with a duration of 10 min. **(a)** is tilt view and **(b)** is top view. The red square is a sample of a part to show how the stage moves. Numbers represent each moving step.

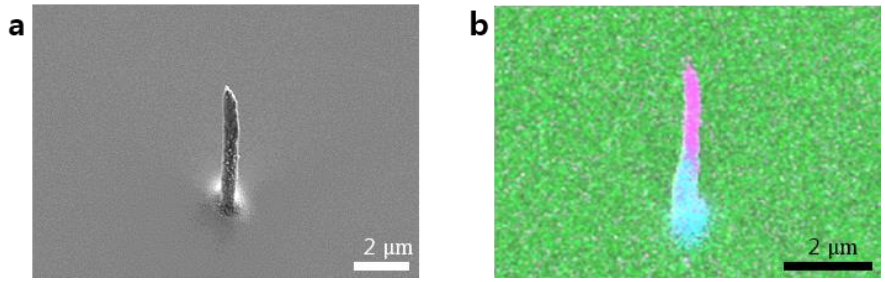

Figure 2.11. Multi-material printing in single fabrication step. (**a**) SEM image and (**b**) EDS map of a nanopillar consisting of Cu at the /bottom (light blue) and Pd on top (pink), implying that the 3D structures can be made from different materials in a single printing process. Green represents Si as the substrate material.

To maximize the capacity of this 3D nanoprinting technique, we adapt the movement of the nanostage in three dimensions while the structures grow. As explained above, the instantaneous tip of the growing structures further focuses the electric field lines; hence, incoming charged particles are exclusively attracted to the tip. Such protrusions offer a largely dominant growth direction (Figure 2.12). In particular, each electric field line (i.e., the nanoparticle trajectory) is determined by both the position of the instantaneous tip and the surface charge density of the floating mask; this essentially transforms the electric field lines into a 3D drawing tool. The proposed 3D nanoprinting technique is the opposite of how Faraday drew electric field lines using a pencil (now we use electric field lines to draw 3D "pencils").

In our aerosol approach, moving the nanostage in 3D can achieve versatile 3D growth of printed nanostructures. As already shown in Figure 2.9, vertical nanopillars are printed by only performing one-dimensional (1D) movement along the *z*-direction. Figure 2.12 and 2.13 show another example of 1D movement of the nanostage along the *x*-axis to print the overhanging 3D nanostructures. To print the overhanging structures with tilted angles of $\theta = 25°, 45°$, and $90°$, we first printed vertical pillar part for 600 s with a fixed distance of 6 μm between the mask and the stage; then, we translated the nanostage along the *x*-axis at different speeds. Figure 2.13 shows that the

translation speed of the nanostage correlates to the angle of the overhanging structures. The structures generally grow upward ($\theta < \pi/2$), whereas counterintuitive downward growth ($\theta \geq \pi/2$) is also realized. Upward growth structures show that their slanted angle ($\theta = 25°,\ 45°$) is controlled by the translational speed of the nanostage (3.3, 5.6 $\mathrm{nm\ s^{-1}}$). After a sudden horizontal movement of the nanostage to a distance of 0.5 μm from the vertical pillar, an orthogonally intersecting structure ($\theta = 90°$) is also obtained at a translating speed of 9.6 $\mathrm{nm\ s^{-1}}$. It should be noted that downward growth must be initiated by instantly choosing a checkmark-like streamline (see the third case in Figure 2.12). To capture this streamline, we must quickly shift the hole center away from the instantaneous tip of the nanopillar, which manipulates the shape of electric field lines and consequently the trajectories of the charged aerosols. Following this principle, we first achieved an upward growth with a tilted angle of $\theta = 55°$ at a translating speed of 6.7 $\mathrm{nm\ s^{-1}}$. Subsequently, we performed a sudden jump of the nanostage to a horizontal distance of 2 μm from the slanted tip. Then, we reduced the nanostage velocity to 4.6 $\mathrm{nm\ s^{-1}}$ to achieve a 160° downward growth, as shown in the bottom pannel of Figure 2.13. Full details of the nanostage movement can be found in Table 2.2 in the end of Chapter 2. The successful printing of the overhanging structures with different

slanted angles lies in the fact that the shape of the guiding electric field lines is determined by the distance between the structure tip and the hole center.

Different to the horizontal nanostage movement, simultaneously moving the nanostage in two dimensions (along *x*-/*z*-axis) enables the printing of zigzag and stair-like 3D nanostructures, as shown in Figure 2.14 and 2.15.

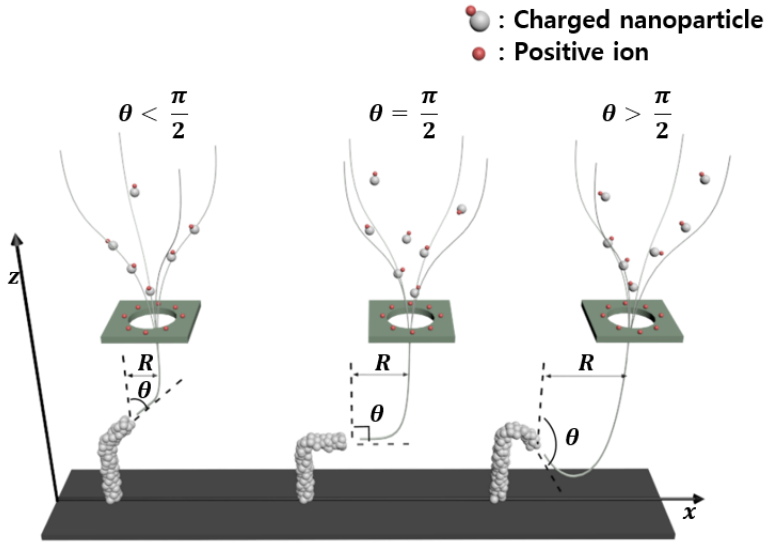

Figure 2.12. Schematic of the process for printing “tip directed growth mode”.

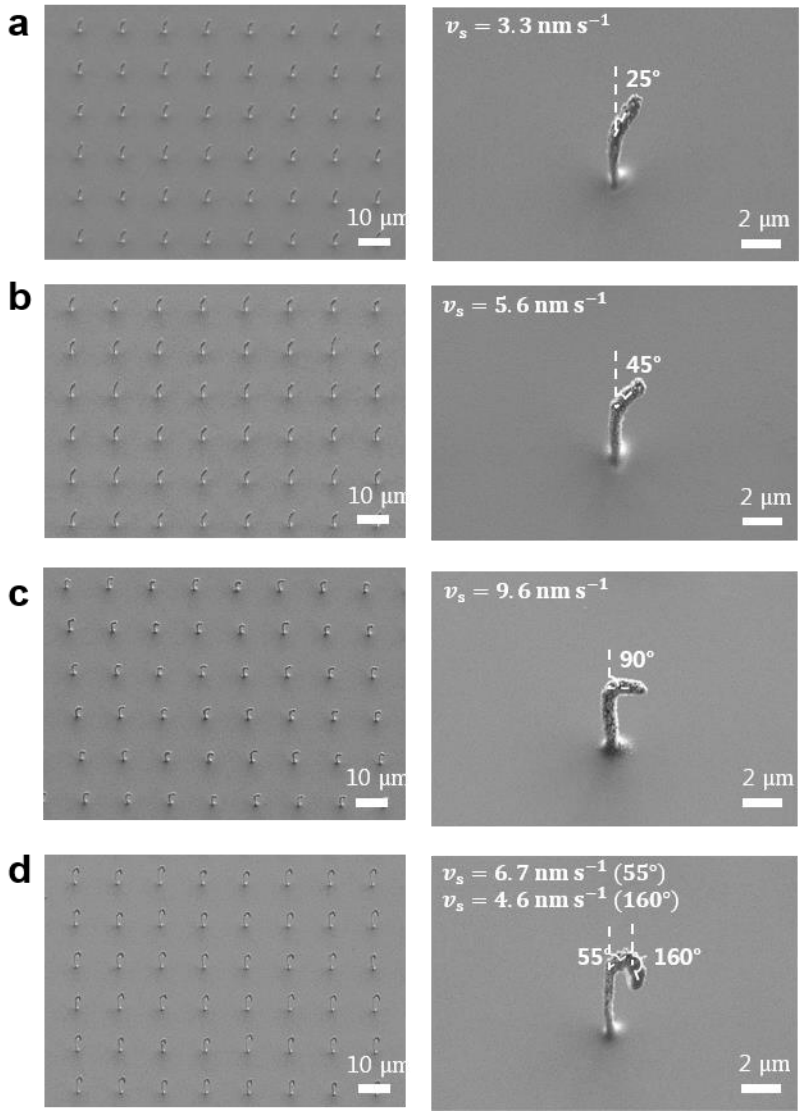

Figure 2.13. The experiment results of "tip-directed growth" depending on the nanostage translation speed to the *x*-axis. The angles of the slanted parts are controlled at **(a)** 25°,**(b)** 45°,**(c)** 90°, and **(d)** 160°.

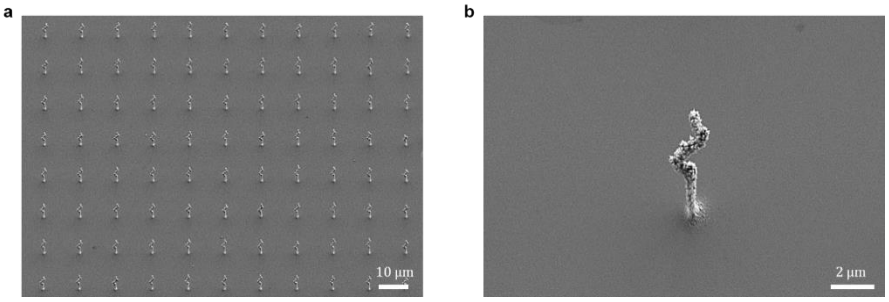

Figure 2.14. SEM images of the 3D zigzag-shaped structures. After initial deposition for 600 s (defined as the origin of the coordinates of the nanostage movement), the piezoelectric nanostage moved to the left by −1 μm along the x-axis with 4.2 $\mathrm{nm\,s^{-1}}$. Then, it moved past the origin and further to the right by 1 μm along the x-axis with 4.2 $\mathrm{nm\,s^{-1}}$. Finally, the nanostage moved back to the origin with 4.2 $\mathrm{nm\,s^{-1}}$ translation speed. The initial distance between the mask and the substrate was 7 μm and after stationary deposition (600 s), the nanostage moved down 2 μm with a velocity of 2.1 $\mathrm{nm\,s^{-1}}$. (**a**) Tilt-view SEM image of an array of zigzag structures. (**b**) Magnified view of a single zigzag structure.

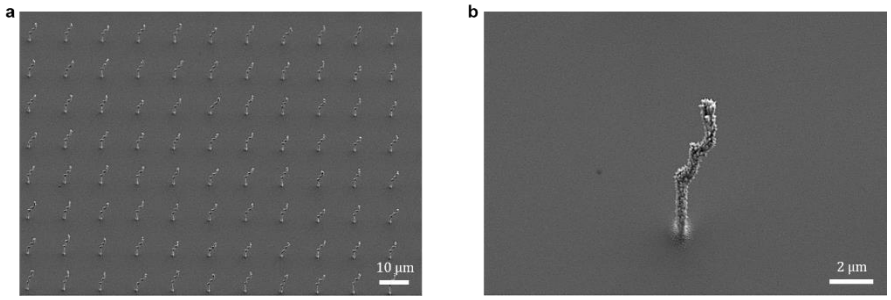

Figure 2.15. SEM images of the 3D stair-like structures. After initial deposition for 600 s, the nanostage jumped a distance of 1 µm from the initial point for 7.5 min of deposition. These two steps are then repeated a second time. The initial distance between the mask and the substrate was 6 µm, and after stationary deposition (600 s) the nanostage moved down 1.5 µm with the velocity of 1.3 $\mathrm{nm\,s^{-1}}$. (**a**) Tilt-view SEM image of the stair-like structures. (**b**) Magnified view of a single stair-like structure.

Besides the 1D and 2D movement of the nanostage, we can also facilitate a 3D movement of the nanostage. This enables the printing of helix structures (cf. Figure 2.16) and provides the cornerstone for even more complex structures. The difference between Figure 2.16a and Figure 2.16b is that the rotational angles are 360° and 180°, respectively. The distance between the floating mask and the substrate was spaced at 6 μm. The nanostage was first kept still for 600 s, and then, it was rotated along an orbit with a radius of 1 μm at an angular velocity of $4\pi\ h^{-1}$ in the *xy*-plane while simultaneously being moved down 3 μm for 1800 s along the *z*-axis. This manipulation allows printing helices with a helix angle of $\theta_t = 41°$, radius of 0.9 μm, and lead of 4.2 μm (Figure 2.16b). The pillar width is 340 nm (about 1/10 of the hole size due to above-mentioned focusing effect) and the bottom vertical pillar has a height of 2.1 μm. More details of the experiment conditions can be found in Table 2.2.

Manufacturing various type of helices is also possible. To obtain versatile shape of helices, we should optimize nanostage translation to the expecting structure shape. Figure 2.17 shows helices have 1/4 diameter of Figure 2.16. The distance between the floating mask and the substrate was spaced at 2 μm. The nanostage was first kept still for 180 s, and then, it was rotated along an orbit with a radius of 250 nm at an angular velocity of $4\pi\ h^{-1}$ in the *xy*-

plane while simultaneously being moved down 3150 nm for 540 s along the z-axis.

After this 1 round miniaturized helices experiment, keeping the nanostage rotation leads to 2 round helices. The difference between Figure 2.18a and Figure 2.18b is that the second round nanostage rotational direction is reversed, respectively.

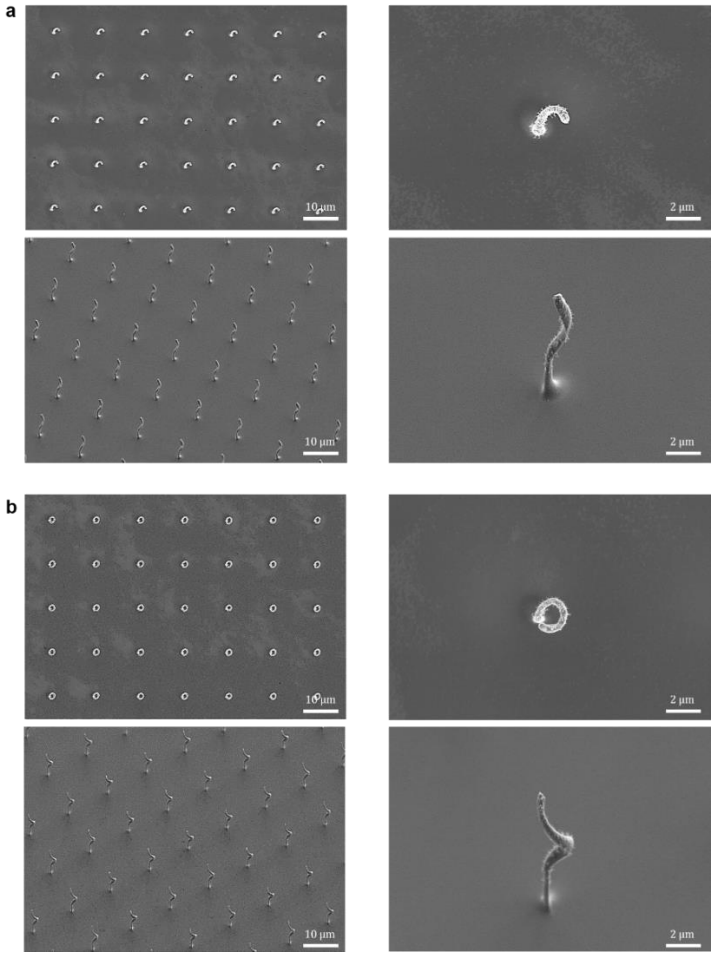

Figure 2.16. SEM images of the helix structures rotated by 180° and 360° The rotation radius of the nanostage was 1 µm, while the constant angular frequency was $4\pi\ h^{-1}$. They are printed by rotating the nanostage. (**a**) The nanostage rotation angle is 180°. Upper side images show top-view SEM images and down side images show tilt-view SEM images. Right side images show magnified view. (**b**)The nanostage rotation angle is 360°. Upper side images show top-view SEM images and down side images show tilt-view SEM images. Right side images show magnified view.

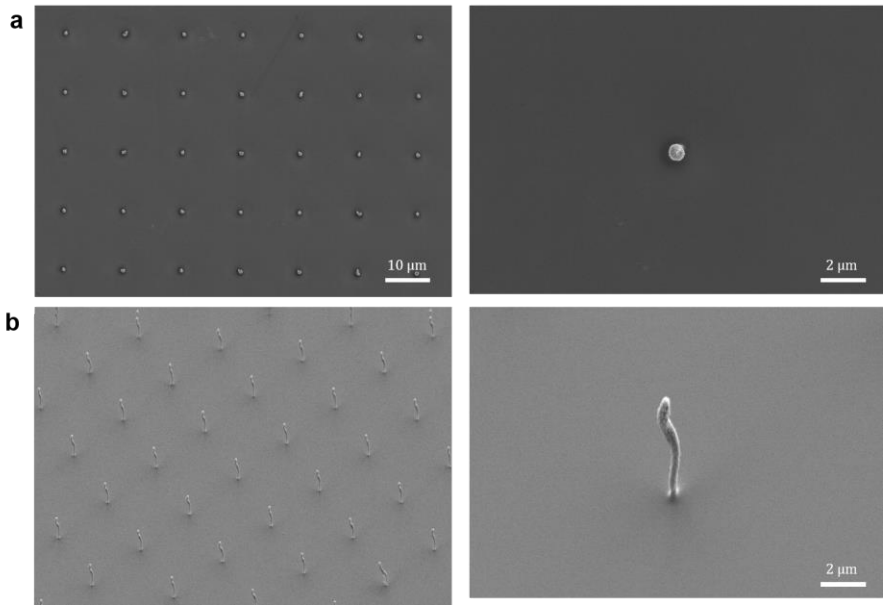

Figure 2.17. SEM images of the helix structures. As shown in the images, the 360° helix has 250nm radius. (**a**) Top-view SEM images. Right side image shows magnified view. (**b**) Tilt-view SEM images. Right side image shows magnified view.

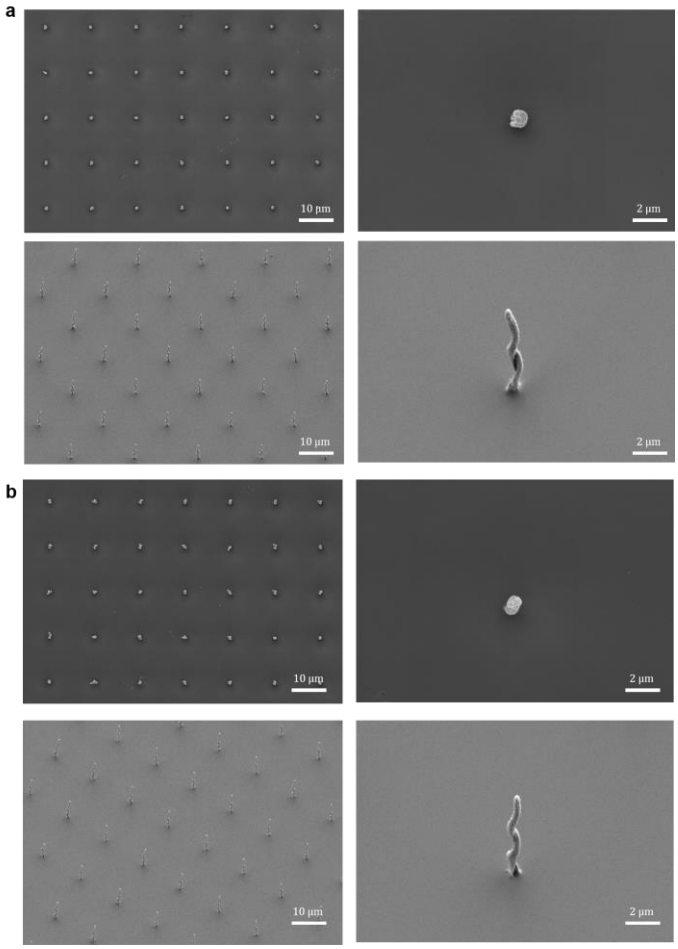

Figure 2.18. SEM images of the helix structures rotated 2 round. The difference between (**a**) and (**b**) is that second round nanostage rotatinal direction is reverse. (**a**) The nanostage rotates 2 round in right-hand direction. Upper side images show top-view SEM images and down side images show tilt-view SEM images. Right side images show magnified view. (**b**)The nanostage rotates left-hand direction after first round rotation in right-hand direction. Upper side images show top-view SEM images and down side images show tilt-view SEM images. Right side images show magnified view.

In addition to the aforementioned pillar-like structures, we also demonstrate printing wall-like structures by using a stationary mask with slits of different shapes. Printing wall-like structures is similar to tip-guided growth, because the tip apexes can spread along the line of the wall. Figure 2.19 shows SEM images of various wall-like structures (the letters SNU in 3D (width: 600 nm, height: 3.5 μm), fallen-over tables (width: 700 nm, height: 3.1 μm), and castle-like (height: 3.2 μm)) printed in this manner. The fabricated shapes of the structures follow the shapes designed on the mask as shown in Table 2.1. However, the growth within each structure is not perfectly uniform along the slit since the converging electric field would not be uniform along the slit due to edge effect and as charged aerosols would follow these field lines. The design of mask patterns should be optimized for producing the exact desired structure.

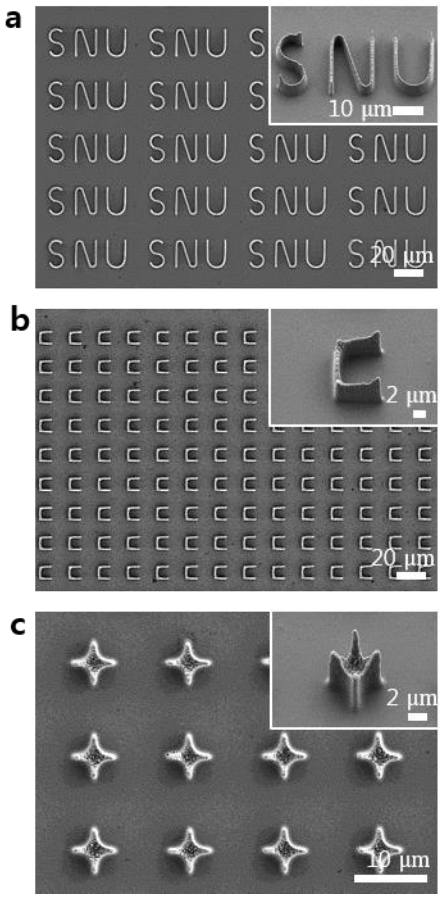

Figure 2.19. The printed wall-like 3D structures (**a**) The letter SNU (abbreviated from Seoul National University), (**b**) a ⊂-shaped holy mask and the resulting fallen-over tables, and (**c**) a four-petal-like holy mask and the printed castle-like structures. Exact dimensions of the mask patterns are provided in the Table 2.1.

2.3.2 Surface writing of 3D metal nanostructure

To show the versatility of our drawing tool, we demonstrate another mode of 3D nanoprinting. When the horizontal velocity of the moving nanostage exceeds the growth rate of the structure, the tip-directed growth mode terminates and charged aerosols do not deposit on top of tip; instead, they deposit on the substrate following the movement of the nanostage. Figure 2.20a shows a nanopillar with a tail on the right side indicating the printing on the substrate (not on the tip of the nanopillar) following the translation of the stage when the nanostage first holds still for 10 min and subsequently moves to the right side quickly at 25 $\mathrm{nm\,s^{-1}}$. This is said to be a "writing mode." By equalizing the translational movement in the *x* and *y* directions, we print ring structures (Figure 2.20b) and according to the programmed nanostage movement we write the letters "3D" (Figure 2.20c). The ring structures are impossible to fabricate using a stationary mask because creating a mask with such ring patterns is unrealistic as the disk at the center of the ring would be detached from the outer circumference. Another interesting feature is that we can print composite structures on the same substrate by depositing another material. For example, in Figure 2.20d, the letter 3 is printed with Cu, and the letter D is printed with Pd. The detailed height and width profiles of the 3D letter structure can be found in Figure 2.21.

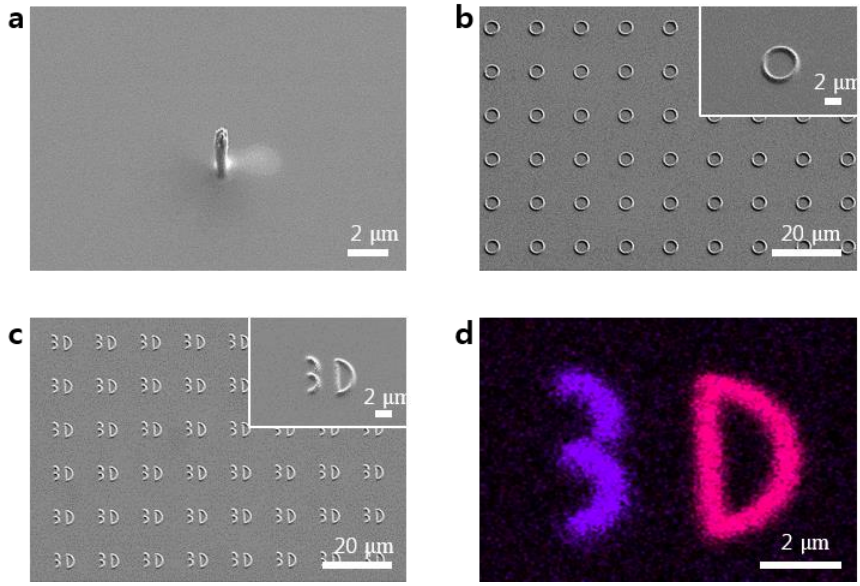

Figure 2.20. Printing in "writing mode." (**a**) Scattered nanoparticles on the right side of a nanopillar. Nanoparticles cannot deposit the existing nanopillar tip when the translational velocity of the nanostage increases over a certain value. After printing for 10 min with a stationary nanostage, the nanostage then translates horizontally at 25 $\mathrm{nm\,s^{-1}}$. (**b**) Ring structures printed by repeatedly moving the nanostage in a circle (**c–d**) Letters written on the substrate through the programmed movement of the nanostage. (**c**) Array of the letters "3D" and their corresponding EDS mapping (**d**), in which Cu is purple, and pink represents Pd.

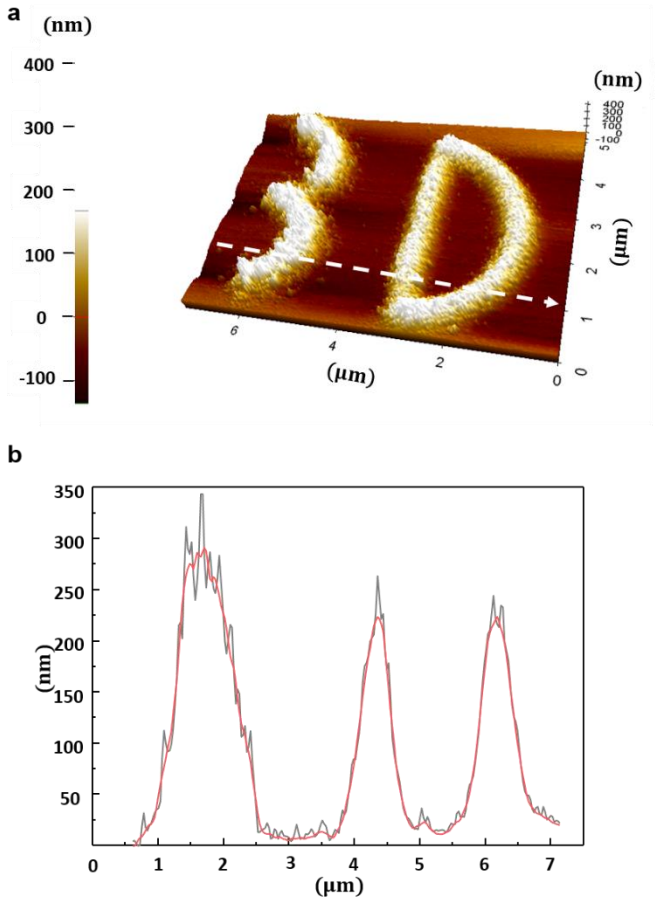

Figure 2.21. (a) Atomic force microscopy topography image of the letters "3D" and (b) the corresponding height profile. The height profile is scanned along the white dashed arrow. For clarity, the measurements are smoothed, as shown in red.

2.3.3 Property analysis of 3D metal nanostructure

To show usefulness of our 3D metal additive manufacturing, we investigate mechanical properties of fabricated nanostructures. It is very important to prove mechanical robustness due to the development in nanodevice field requires outstanding quality of metal nanostructures.

Owing to the fully dry process, the printed 3D metal nanostructures rarely have impurities. The energy dispersive X-ray spectroscopy (EDS) show that the nanopillar has highly pure Pd nanoparticles (see EDS data in Figure 2.22). The exclusively high purity of metal nanostructure has much possibility to having a high electrical conductivity. However, the van der waals force is dominant force to nanoparticles to forced to maintaining the shape of structure, sintering process is essential to form more crystalline structure after manufactured 3D metal nanostructures. As shown in the Figure 2.23, the thermal sintered structures on the 200°C hot plate during 2 hours have only 5 times higher resistivity than bulk Pd. For the accurate electrical conductivity measurement, the structures are broken by tweezer after manufactured on the Si substrate have 500 nm thickness SiO_2 on the top of the surface thorugh the thermal evaporation process. After that 4 point nanoprobe conducted analysis. The sintering process also increase the mechanical strength of nanostructures. The highest hardness of structure is obtained when the structures are sintered on the 200°C hot plate during 2 hours. The structure maintains own shape until stress becomes around 630 MPa and at this point the structures indicates 10.5 GPa of elastic modulus.

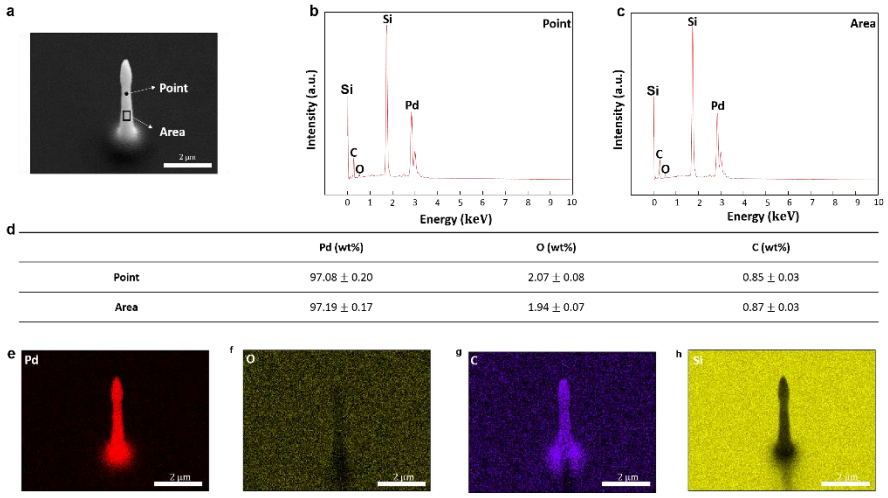

Figure 2.20. EDS analysis of a single nanopillar. (**a**) SEM image of a nanopillar. Point and area EDS spectra are shown in (**b**) and (**c**), respectively. (**d**) The nanopillar has almost pure Pd (more than 97 wt%) since O and C are always present from the sample exposure to the environment. This %wt data is averaged value of 10 nanopillars. We excluded the substrate material Si. (**e**)- (**h**) EDS maps of Pd, O, C, and Si.

a

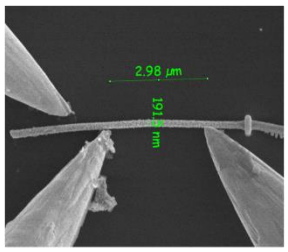

b

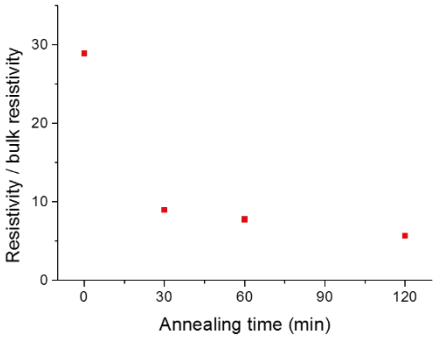

c

Sintering time	0	30min	1hr	2hr
ρ (nΩ · m)	3045.22	948.12	818.17	596.6

Bulk Pd: 105.4 nΩ · m

Figure 2.21. The analysis data of electrical conductivity measurement of Pd nanopillar. (**a**) Captured SEM image during analysis. (**b**) Comparison between the resistivity of Pd nanopillar to the bulk resistivity of Pd depending on the sintering time. (**c**) The resistivity of Pd nanopillar depending on the sintering time.

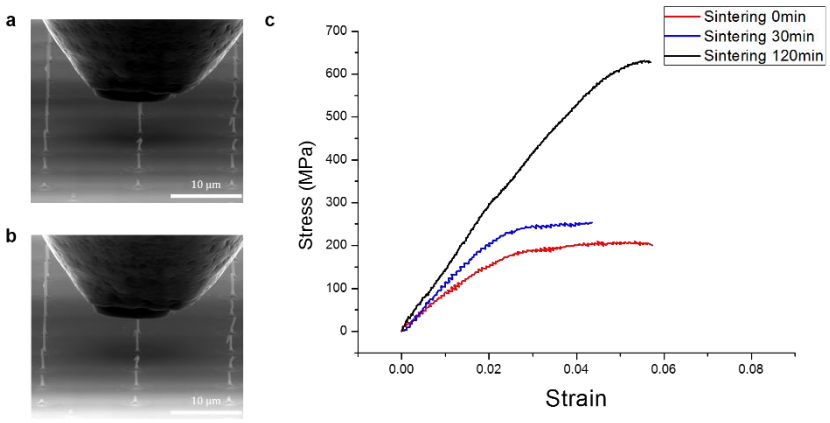

Figure 2.22. The mechanical hardness data of Pd nanopillar. 10 μm diameter Nanoindentation tip is used for analysis. (**a**) SEM image before Nanoindentation measure the mechanical hardness of Pd nanopillar. (**b**) SEM image after measurement. Broken nanopillar is shown. (**c**) Stress-strain graph shows mechanical hardness data depending on the structure sintering time. The highest strength is shown when the structure sintered during 120 min. At this condition the structure tolerate 630 MPa and has 10.5 GPa elastic modulus.

Table 2.1. Dimensions of floating mask patterns. A, B, and C are marked on the SEM images at bottom.

Mask pattern geometry	Si_3N_4 thickness (μm)	Opening area (μm^2)	Pitch		Diameter (μm)	Slit width (μm)	C (μm^2)
			A (μm)	B (μm)			
Hole	1	750 × 750	13	13	4	-	-
SNU	1	750 × 750	68.7	36	-	3	55.7 × 23.1
Fallen-over table	1	750 × 750	20	20	-	3	11.5 × 11.5
Temples	1	750 × 750	13	13	-	3	9 × 9

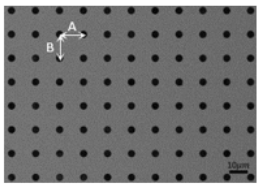

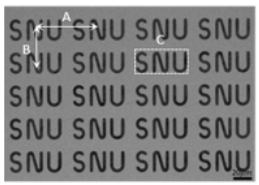

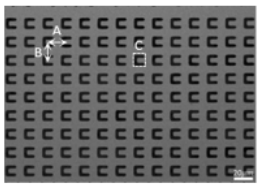

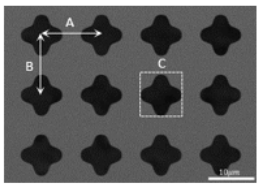

Table 2.2. Experimental conditions in 3D nanoprinting

Structures		Initial vertical distance (μm)	Nanostage traveling distance		Nanostage speed		Growth time		Growth rate		Dimensions		Width (μm)
			Vertical (μm)	Horizontal x_s (μm)	Vertical (nm/s)	Horizontal v_s (nm/s)	Still (s)	Moving (s)	Total (nm/s)	Slanted v_g (nm/s)	Vertical (μm)	Slanted (μm)	
Vertical pillars (Fig. 1D)		7	9	-	10.0	-	600	900	7.3	-	11	-	0.30
Overhangs (Fig. 2B)	25°	6	-	1	-	3.3	600	300	5.2	7.7	2.4	2.3	0.64
	45°	6	-	2	-	5.6	600	360	5.0	6.7	2.4	2.4	0.58
	90°	6	-	2.6 (including jump 0.5)	-	9.6	600	220	5.9	10.0	2.6	2.2	0.75
	55°+ 160°	7	-	1.3[a)] 2.6 (including jump 2)[b)]	-	6.7[a)] 4.6[b)]	660	195[a)] 130[b)]	6.6	7.7[a)] 9.2[b)]	3.2	1.5[a)] 1.2[b)]	0.42
Wall-like (Fig. 4)	SNU	4	1	-	0.8	-	3600	1200	0.7	-	3.5	-	0.55
	Fallen-over table	4	1	-	0.8	-	3600	1200	0.7	-	3.2	-	0.40
	Castles	4	1	-	0.8	-	3600	1200	0.8	-	3.6	-	0.64
Writing mode (Fig. 5, A to C)	Pillar	7	-	2.5	-	25	600	100	4.0	-	2.4	-	0.63
	Ring	7	-	4π × 30	-	100	-	3770	-	-	-	-	-
	3	7	-	1.83π × 63	-	100	-	3622	-	-	-	-	-
	D	7	-	(2π+4) × 35	-	100	-	3600	-	-	-	-	-

Structures	Initial vertical distance (μm)	Nanostage traveling parameters			Nanostage speed		Growth time		Growth rate		Dimensions		Width (μm)
		Vertical (μm)	Radius R_s (μm)	Rotation angle (°)	Vertical (nm/s)	Angular velocity ω (/h)	Still (s)	Moving (s)	Total (nm/s)	Cycle v_g (nm/s)	Vertical (μm)	Cycle (μm)	
Helix (Fig. 3)	6	3	1	360	1.7	4π	600	1800	3.9	4.1	2.1	7.3	0.34

a) Upward slanted part (55°); b) Downward slanted part (160°)

2.4 Summary

In this chapter, we have introduced a powerful, flexible 3D nanoprinting technology using charged aerosols as building blocks. This completely dry and parallel technique implements electric field lines as a drawing tool under atmospheric condition. Notably, such a tool equipped with nanoscopic electrostatic lens in principle has eliminated the physical size restrictions encountered in other 3D printing technologies, thus paving the way for further downscaling. To demonstrate the material flexibility of the nanoparticle source, we print hybrid structures consisting of Pd and Cu. We have also shown that 3D nanoprinting can operate in two complementary modes: tip-directed 3D growth and surface writing. The former facilitates the printing of nanopillar/wall-like structures (e.g., vertical/overhanging nanopillars, helices), while the latter enables writing ring structures and letters. Furthermore, the mechanical property data of electrical conductivity and mechanical hardness show possibility to the versatile applications in the nanotechnology field.

Wooik Jung and Yoon-ho Jung equally contributed in this work.

2.5 References

[1] Kim, H., Kim, J., Yang, H., Suh, J., Kim, T., Han, B., Kim, S., Kim, D. S., Pikhitsa, P. V., Choi, M. Parallel patterning of nanoparticles via electrodynamic focusing of charged aerosols. *Nat. Nanotechnol.* **1**, 117–121 (2006).

[2] Lee, H., You, S., Woo, C. G., Lim, K., Jun, K., Choi, M. Focused patterning of nanoparticles by controlling electric field induced particle motion. *Appl. Phys. Lett.* **94**, 053104 (2009).

[3] You, S., Han, K., Kim, H., Lee, H., Woo, C. G., Jeong, C., Nam, W., Choi, M. High-resolution, parallel patterning of nanoparticles via an ion-induced focusing mask. *Small* **6**, 2146–2152 (2010).

[4] Lee, H., You, S., Pikhitsa, P. V., Kim, J., Kwon, S., Woo, C. G., Choi, M. Three-dimensional assembly of nanoparticles from charged aerosols. *Nano Lett.* **11**, 119–124 (2011).

[5] Feng, J. C., Guo, X. A., Ramlawi, N., Pfeiffer, T.V., Geutjens, R., Basak, S., Nirschl, H., Biskos, G., Zandbergen, H.W., Schmidt-Ott, A. Green manufacturing of metallic nanoparticles: a facile and universal approach to scaling up. J. Mater. Chem. A 4, 11222–11227 (2016).

[6] Tabrizi, N. S., Ullmann, M., Vons, V.A., Lafont, U., Schmidt-Ott, A. Generation of nanoparticles by spark discharge. J. Nanopart. Res. 11,

315–332 (2009).

[7] Bae, Y., Pikhitsa, P. V., Cho, H., Choi, M. Multifurcation assembly of charged aerosols and its application to 3D structured gas sensors. *Adv. Mater.* **29**, 1604159 (2017).

[8] Ha, Kyungyeon, et al. "A light-trapping strategy for nanocrystalline silicon thin-film solar cells using three-dimensionally assembled nanoparticle structures." *Nanotechnology* 27.5 (2016): 055403.

[9] Jung, K., Hahn, J., In, S., Bae, Y., Lee, H., Pikhitsa, P. V., Ahn, K., Ha, K., Lee, J. K., Park, N., Choi, M. Hotspot-engineered 3D multipetal flower assemblies for surface-enhanced Raman spectroscopy. *Adv. Mater.* **26**, 5924–5929 (2014).

Chapter 3.

Numerical and Mathematical Analysis of 3D metal nanostructure growth

3.1 Introduction

We have introduced ion assisted aerosol lithography based 3D metal nanoprinting and diverse nanostructures with high controllability. High-aspect ratio nanopillar, overhanging structures with diverse angles and helices show new approach to the metal additive manufacturing in nanoscale resolution. To support this versatile 3D drawing tool, we conduct theoretical analysis of structural growth in our aerosol approach.

Firstly, we analyze trajectory of charged nanoparticle which is building block in this lithotraphy. Because, 3D nanostructures are consist of accumulated nanoparticles, predicting a trajectory of nanoparticle affects shape of desired nanostructures. MATLAB was used to solve the Langevin's equation which is consist of various forces affecting airborne nanoparticles and the trajectory simulated results suit well with manufactured nanostructures.

Secondly, we develop powerful phenomenological model for structural growth. It is assumed that all charged nanoparticles follow guiding electric field line to floating mask opening and are attracted together to the structure tip. The manufactured structure is also negligible so we only consider the tip of structure. Building upon this, the model is derived from electric field flux

conservation equation and calculated results show similar shape to the real structure.

3.2 Simulation of particle trajectory by solving Langevin's equation

MATLAB was used to simulate the particle trajectories [1]. Langevin's equation, which contains the sum of various forces **F** (e.g., drag force $\mathbf{F}_\mathrm{D}$, external force $\mathbf{F}_\mathrm{E}$) and a noise term representing random collisions, i.e., Brownian diffusion force $\mathbf{F}_\mathrm{B}$, was employed. The equation can be rewritten as

$$m_\mathrm{p}\frac{d\mathbf{v}_\mathrm{p}}{dt} = \mathbf{F} + \mathbf{F}_\mathrm{B}$$

where m_p is the mass of a particle, $\mathbf{v}_\mathrm{p}$ is the particle velocity, and $\mathbf{F}_\mathrm{E}$ consists of the Coulomb force ($\mathbf{F}_\mathrm{C}$), image force ($\mathbf{F}_\mathrm{Im}$), dipole force($\mathbf{F}_\mathrm{Di}$), and van der Waals force ($\mathbf{F}_\mathrm{vdW}$). Considering the correlation between $\mathbf{v}_\mathrm{p}$ and the traveling distance, the trajectory of charged nanoparticles can be derived from the above equation. The drag force $\mathbf{F}_\mathrm{D}$ is given by

$$\mathbf{F}_\mathrm{D} = f(\mathbf{v}_\mathrm{g} - \mathbf{v}_\mathrm{p})$$

where $\mathbf{v}_\mathrm{g}$ is the gas velocity and f is the friction coefficient, $3\pi\mu d_\mathrm{p}/C_\mathrm{C}$; μ is the viscosity of the gas; d_p is the particle diameter; and C_C is the Cunningham correction factor [2]. $\mathbf{F}_\mathrm{C}$ is given by

$$\mathbf{F}_\mathrm{C} = q\mathbf{E}$$

where q is the charge of the particle and $\mathbf{E}$ is the electric field calculated using the surface charge density ($5.7 \times 10^{-6}\ \mathrm{C/m^2}$), substrate voltage ($-1500$ V), and upper boundary voltage (-1497.1 V), which in turn are calculated using COMSOL 5.1. $\mathbf{F}_{\mathrm{Im}}$ is the image force that affects the charged particle.

$$\mathbf{F}_{\mathrm{Im}} = \frac{q^2}{4\pi\varepsilon_{\mathrm{g}}(2D_{\mathrm{C-S}})^2}\frac{\varepsilon_{\mathrm{p}} - \varepsilon_{\mathrm{s}}}{\varepsilon_{\mathrm{p}} + \varepsilon_{\mathrm{s}}}\mathbf{n} + \frac{{d_{\mathrm{p}}}^2 q^2}{\pi\varepsilon_{\mathrm{g}}}\left(\frac{1}{8{D_{\mathrm{C-C}}}^2} - \frac{2D_{\mathrm{C-C}}}{(4{D_{\mathrm{C-C}}}^2 + {d_{\mathrm{p}}}^2)^2}\right)\mathbf{r}$$

where $D_{\mathrm{C-S}}$ is the distance between the center of the particle and the substrate surface and $D_{\mathrm{C-C}}$ is the distance between the centers of the two particles [3,4]. ε_{p}, ε_{s}, and ε_{g} are the relative dielectric constants of the particle, substrate, and gas, respectively [5,6]. $\mathbf{n}$ is the normal vector to the substrate and $\mathbf{r}$ is the directional normal vector between the incoming particles and the particles deposited on the substrate. Dipole force $\mathbf{F}_{\mathrm{Di}}$ is expressed as

$$\mathbf{F}_{\mathrm{Di}} = \mathbf{p}_{\mathrm{eff}} \cdot \nabla\mathbf{E}$$

Here, $\mathbf{p}_{\mathrm{eff}}$ is the effective dipole moment of a particle, $1/2\pi\varepsilon_{\mathrm{g}}K{d_{\mathrm{p}}}^3\mathbf{E}$, where K is the Clausius–Mossotti function, and $\mathbf{F}_{\mathrm{vdW}}$ is the van der Waals force given by

$$\mathbf{F}_{\mathrm{vdW}} = \frac{A_{\mathrm{Hpgs}} {d_{\mathrm{p}}}^3}{12(D_{\mathrm{C-S}} - (d_{\mathrm{p}}/2))^2 (D_{\mathrm{C-S}} + (d_{\mathrm{p}}/2))^2}\mathbf{n} + \frac{A_{\mathrm{Hpgp}} {d_{\mathrm{p}}}^6}{6(D_{\mathrm{C-C}} - d_{\mathrm{p}})^2 {D_{\mathrm{C-C}}}^3 (D_{\mathrm{C-C}} + d_{\mathrm{p}})^2}\mathbf{r}$$

where A_{Hpgs} is the Hamaker constant between the particle and the substrate and A_{Hpgp} is the Hamaker constant between the particles in a gas. The Brownian diffusion force $\mathbf{F}_{\mathrm{B}}$ at each time step is expressed by

$$\mathbf{F}_{\mathrm{B}} = \sqrt{\frac{2k_{\mathrm{B}}Tf}{\Delta t}}\boldsymbol{\zeta}$$

where k_{B} is the Boltzmann constant (1.381×10^{-23} J/K), T is the temperature (293 K), t is time, and $\boldsymbol{\zeta}$ is a vector consisting of the zero-mean, unit variance Gaussian random numbers [7].

The surface potential distribution of accumulated ions can be estimated from the KFM measurements (cf. Figure 2.8). To simulate the overhanging structures, the total translation distance was determined using experimental data (cf. Table 2.2). The number of nanoparticles for each step simulation was regulated by the deposition time (25°: 6816 particles per 15 min, 45°: 6965 particles per 16 min). Such numbers were based on the growth rate of the structures for a particle size of 10 nm. These simulation results for the particle trajectory are comparable to those obtained from the phenomenological model and from the experiments. Therefore, the shape of

the structures can also be described by the particle trajectories (simulation results are in Figure 3.1).

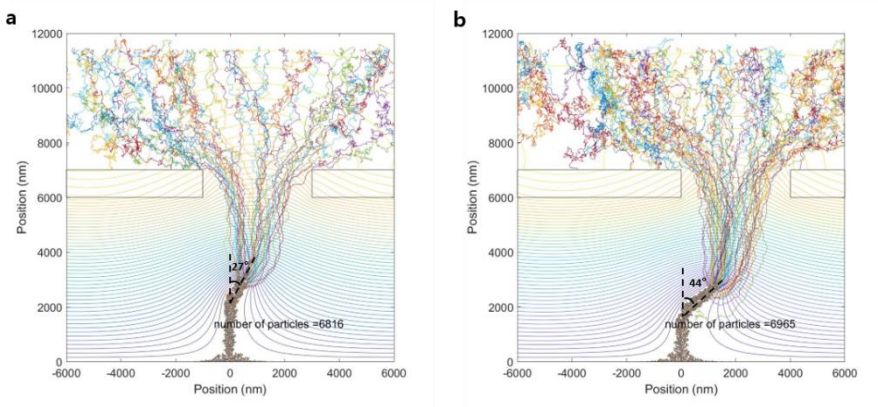

Figure 3.1. Particle trajectory simulation results of overhanging structures. Simulation of nanoparticle trajectories in case of (**a**) 25°, (**b**) 45°. The simulation result agrees well with the experiment result shown at the Figure 2.13.

3.3 Phenomenological model for structural growth

We develop a phenomenological model to describe the structure growth. For the case of overhanging structures in Figure 2.12 and 3.2, the tip growth rate along the x- and z- directions can be expressed as

$$\frac{\mathrm{d}x_{\mathrm{tip}}}{\mathrm{dt}} = v_{\mathrm{g}} \sin\theta(\mathrm{t}),\ \frac{\mathrm{d}z_{\mathrm{tip}}}{\mathrm{dt}} = v_{\mathrm{g}} \cos\theta(\mathrm{t}) \qquad (1)$$

where x_{tip} and z_{tip} are the *x*- and *z*-axis position of the tip, v_{g} is a growth rate of the structure, and $\theta(\mathrm{t})$ $(0 \leq \theta(\mathrm{t}) \leq \pi)$ is the time dependent angle between the guiding streamline and the z-axis. In the model, we assumed that charged aerosols follow the guiding electric field line that starts from the hole center of the mask (x_{s}) and terminate at the structure tip (x_{tip}). This guiding streamline is shown in Figure 2.12. By applying the electric field flux conservation principle and using experimentally determined v_{g}, the governing equation for $\theta(\mathrm{t})$ can be derived to determine $x_{\mathrm{tip}}(\mathrm{t})$ and $z_{\mathrm{tip}}(\mathrm{t})$ by solving Eq. (1). The overhanging structures are then predicted from $x_{\mathrm{tip}}(\mathrm{t})$ and $z_{\mathrm{tip}}(\mathrm{t})$ and compared with experiments in Figure 3.2 showing good agreement between the experimental results and the model predictions for four representative angles ($\theta =$ 25°, 45°, 90°, and 160°).

With respect to the case of helices, the full 3D tip growth is governed by the following three equations

$$\frac{\mathrm{d}x_{\mathrm{tip}}}{\mathrm{dt}} = v_{\mathrm{g}} \sin\theta(\mathrm{t}) \cos\psi(\mathrm{t}),\ \frac{\mathrm{d}y_{\mathrm{tip}}}{\mathrm{dt}} = v_{\mathrm{g}} \sin\theta(\mathrm{t}) \sin\psi(\mathrm{t}),\ \frac{\mathrm{d}z_{\mathrm{tip}}}{\mathrm{dt}} = v_{\mathrm{g}} \cos\theta(\mathrm{t}) \tag{2}$$

where $\cos\psi(\mathrm{t}) = (x_{\mathrm{s}} - x_{\mathrm{tip}})/R$, $\sin\psi(\mathrm{t}) = (y_{\mathrm{s}} - y_{\mathrm{tip}})/R$ and $R = \sqrt{(x_{\mathrm{s}} - x_{\mathrm{tip}})^2 + (y_{\mathrm{s}} - y_{\mathrm{tip}})^2}$.

We solve Eq. (2) to obtain the position of the helix tip according to the nanostage rotation parameters.

Helices are printed by rotating the nanostage in the *xy* plane with a rotational radius R_{s} at a constant angular velocity ω. Despite the continuous rotation of the nanostage, the helix growth cannot respond immediately when starting growth, and thus, it has a delayed angle. This delayed angle causes a smaller helix radius R_{tip} than R_{s}, as shown in Figure 3.3. When the helix growth reaches a steady state, the geometry can be described by constant parameters (angular velocity of helix growth: ω, helix angle: θ_{t}, and delayed angle: φ). In Figure 3.3, the black circle represents the rotational track of the hole center, while the red spiral corresponds to the expected helix growth after reaching steady-state. Following the above theoretical approach, we obtain similar prediction of helix structure to those measured from SEM images (cf. Figure 3.4).

To be more specific, the geometry of the guiding line can be calculated as follows. It is assumed that all electric field lines flow normally from the mask surface and are bunched together while focusing at the tip of the equipotential growing structure. The simplest phenomenological picture is obtained when only the tip is considered while neglecting the growth structure and the substrate. Then, it is easy to notice that the line bunching/focusing is governed by the electric field flux conservation equation

$$\pi R^2 \sigma = \frac{q}{4\pi} \int_0^{\theta(\mathrm{t})} 2\pi \sin\theta d\theta = q \frac{1-\cos\theta(\mathrm{t})}{2} \tag{3}$$

where R is the distance from the tip to the hole center along the *x*-axis; $\theta(\mathrm{t})$ is the angle between the normal/vertical *z* direction and the guiding line; σ is the surface charge density on the mask, and q is the effective "charge" on the equipotential tip surface that gives the phenomenological description of the line focusing on the tip. Eq. (3) can be rewritten conveniently as

$$R = L_{\mathrm{p}} \sin\frac{\theta(\mathrm{t})}{2} \tag{4}$$

where $L_{\mathrm{p}} = \sqrt{(q/\pi\sigma)}$ is the phenomenological "persistence" length that determines the strength of the focusing. We choose the term "persistence" length because of the analogy with the elastic behavior, while we use the guiding electric field line as a flexible writing rod [9]. We also recall the length

of the charge screening because the electric field lines from charge q are located within the disk of radius L_p on the mask. L_p is an important empirical parameter that (via Eq. (4)) defines the shape of our writing tool, the electric field line.

We compared this simple phenomenology with the COMSOL calculations, by varying the angle θ of the slanted structure and defining R. The dependence closely matches Eq. (4) with the best fit value $L_\mathrm{p} = 1.9\ \mu\mathrm{m}$ (Figure 3.5a). On the other hand, we can approximately recalculate L_p directly from the distribution of the equipotential lines in Figure 3.5b and c. Indeed, the electric field strength along the streamline near the surface of the mask is $E_\sigma = \Delta V/\Delta z_\sigma$, where $\Delta V = 0.1\ \mathrm{V}$ is the potential drop between two equipotential lines in Figure 3.5b and c, and Δz_σ is the distance between them. The field near the tip is $E_\mathrm{tip} = \Delta V/\Delta z_\mathrm{tip}$ with the same potential drop. We recalculate the phenomenological charge $q = E_\mathrm{tip} {r_\mathrm{tip}}^2$, where r_tip is the effective tip radius. This effective radius (as shown in Figure 3.5b and c with the red circle) may be larger than the real tip radius because, effectively, the field lines are perpendicular to the equipotential lines, and they are not concentrated on the tip but in the center of the red circle, which is the effective tip. With the mask charge density $\sigma = E_\sigma/(2\pi)$, we get an estimate

(5)

$$L_{\mathrm{p}} = \sqrt{\frac{q}{\pi\sigma}} = r_{\mathrm{tip}}\sqrt{\frac{2\Delta z_{\sigma}}{\Delta z_{\mathrm{tip}}}}$$

For the most distorted case of downward growth in Figure 3.5b, where the effective tip radius is four times larger than the real tip radius of $250\ \mathrm{nm}$, we obtain from Eq. (5) the value $L_p \approx 1.9\ \mu\mathrm{m}$ to be compared with $L_{\mathrm{p}} \approx 3.2\ \mu\mathrm{m}$ defined from Eq. (4) for this case. Let us consider another example, given in Figure 3.5c, that has $R = 0.45\ \mu\mathrm{m}$ and $\theta = 21°$, thus $L_{\mathrm{p}} \approx 2.5\ \mu\mathrm{m}$. On the other hand, the value obtained from Eq. (5) gives $L_p \approx 1.1\ \mu\mathrm{m}$, which looks reasonably correlated, considering the complexity of the entire field configuration in COMSOL simulation. Note that, to control the entire structure growth, we need only one empirical value of L_{p} in Eq. (4). This greatly simplifies obtaining a protocol for the stage motion for printing complex 3D structures. Therefore, we can predict the shapes of the structures using Eq. (4) and each growth equation of the structures.

In the overhanging structures' cases, Eq. (1), which is the tip growth equation, and Eq. (4) can be rewritten for the tip position x_{tip} in the general case of an arbitrary stage position x_{s} as

$$\frac{\mathrm{d}x_{\mathrm{tip}}}{\mathrm{dt}} = v_{\mathrm{g}} \sin\left(2\, a\sin\left(\frac{x_{\mathrm{s}} - x_{\mathrm{tip}}}{L_{\mathrm{p}}}\right)\right) \tag{6}$$

$$\frac{\mathrm{d}z_{\mathrm{tip}}}{\mathrm{dt}} = v_{\mathrm{g}} \cos\left(2\, a\sin\left(\frac{x_{\mathrm{s}} - x_{\mathrm{tip}}}{L_{\mathrm{p}}}\right)\right) \tag{7}$$

where v_g is the growth rate of the structure and $R = x_s - x_{tip}$. The initial condition shown in Figure 3.2 for solving Eq. (6) is $x_{tip} = 0$ and x_s is determined by v_s. After solving Eq. (6), the shapes of the overhanging structures can be drawn by integrating Eq. (7) with the solution of Eq. (6). In the predicted images and the experiment results, the slanted angle $\theta(t)$ gradually increases from 0 and reaches a constant velocity. For cases when the growth rate becomes nearly constant, one may also define the response time τ. To clarify the physical meaning of response time τ, we use R and v_s. Along the x-axis, the constant translational speed of the nanostage can be expressed as $v_s = v_g \sin\theta_s$, where θ_s is a saturation angle. The tip growth rate along the *x*-directions can thus be expressed as

$$\frac{dR}{dt} = v_s - v_g \sin\theta = v_g \sin\theta_s - v_g \sin\theta \tag{8}$$

Substituting Eq. (4) into Eq. (8), we arrive at

$$\frac{dR}{dt} = L_p \frac{d}{dt} \sin\frac{\theta(t)}{2} \tag{9}$$

If we set Eq. (8) equal to Eq. (9), the equation can be rewritten as

$$\frac{d}{dt} \sin\frac{\theta(t)}{2} = \frac{1}{\tau} (\sin\theta_s - \sin\theta(t)) \tag{10}$$

and we define the response time as $\tau = L_p / v_g$.

In the helix structures cases, from Eqs. (2) and (4), the dimensionless equations for the tip motion of the nanostage motion that rotates along the radius of the nanostage R_s with the constant angular frequency ω are

$$\frac{\mathrm{d}X}{\mathrm{d}T} = \frac{\sin\left(2\,a\sin\left(\left|\vec{\rho}_\mathrm{s} - \vec{\rho}_\mathrm{tip}\right|\Delta\right)\right)}{\Delta}\frac{\left(\vec{\rho}_\mathrm{s} - \vec{\rho}_\mathrm{tip}\right)_x}{\left|\vec{\rho}_\mathrm{s} - \vec{\rho}_\mathrm{tip}\right|} \tag{11}$$

$$\frac{\mathrm{d}Y}{\mathrm{d}T} = \frac{\sin\left(2\,a\sin\left(\left|\vec{\rho}_\mathrm{s} - \vec{\rho}_\mathrm{tip}\right|\Delta\right)\right)}{\Delta}\frac{\left(\vec{\rho}_\mathrm{s} - \vec{\rho}_\mathrm{tip}\right)_y}{\left|\vec{\rho}_\mathrm{s} - \vec{\rho}_\mathrm{tip}\right|} \tag{12}$$

where dimensionless coordinates $X = x_\mathrm{tip}/R_\mathrm{s}$; $Y = y_\mathrm{tip}/R_\mathrm{s}$; $T = t/\tau$; $\Delta = R_\mathrm{s}/L_\mathrm{p}$; $\vec{\rho}_\mathrm{tip} = (X, Y)$; and $\vec{\rho}_\mathrm{s} = (\sin(\omega T + \varphi_0), 1 - \cos(\omega T + \varphi_0))$ when it starts at the phase angle φ_0 (for rotational motion configuration, see Figure 3.6). $\cos\psi(\mathrm{t}) = (x_\mathrm{s} - x_\mathrm{tip})/R = \left(\vec{\rho}_\mathrm{s} - \vec{\rho}_\mathrm{tip}\right)_x/\left|\vec{\rho}_\mathrm{s} - \vec{\rho}_\mathrm{tip}\right|$ and $\sin\psi(\mathrm{t}) = (y_\mathrm{s} - y_\mathrm{tip})/R = \left(\vec{\rho}_\mathrm{s} - \vec{\rho}_\mathrm{tip}\right)_y/\left|\vec{\rho}_\mathrm{s} - \vec{\rho}_\mathrm{tip}\right|$ in Eq. (2). The initial conditions for computation shown in Figure 2.16b is $X = 0$, $Y = 0$. The vertical tip coordinate is calculated from the solution of Eqs. (11) and (12) as

$$Z = \int_0^T \frac{\cos\left(2\,a\sin\left(\left|\vec{\rho}_\mathrm{s} - \vec{\rho}_\mathrm{tip}\right|\Delta\right)\right)dT}{\Delta} \tag{13}$$

where $Z = z_{\mathrm{tip}}/R_{\mathrm{s}}$. One can show by disturbing Eqs. (11) and (12) that the downwards growth of the steady state helix is stable at any parameters, unlike the 1D case considered above.

To derive the $R_{\mathrm{tip}}/R_{\mathrm{s}}$ and θ_{t} of the helix for predicting the radius of the structure and the helix angle, we write the following equations from Figure 3.3a and b. From Figure 3.3a and b, we obtain: $R = R_{\mathrm{s}} \sin\varphi = L_{\mathrm{p}} \sin(\theta_{\mathrm{t}}/2)$, $R_{\mathrm{tip}} = R_{\mathrm{s}} \cos\varphi$, and $R_{\mathrm{tip}}\omega = v_{\mathrm{g}} \sin\theta_{\mathrm{t}}$. Here, φ is the delayed angle between the tip and the hole, θ_{t} is the helix angle, and R has the same meaning as it does in Eq. (4), i.e., it is distance between the tip and the hole center.

Multiplying τ by $R_{\mathrm{tip}}\omega = v_{\mathrm{g}} \sin\theta_{\mathrm{t}}$ and substituting $R_{\mathrm{tip}} = R_{\mathrm{s}} \cos\varphi$, we obtain

$$R_{\mathrm{s}} \cos\varphi = \frac{L_{\mathrm{p}}}{W} \sin\theta_{\mathrm{t}} \tag{14}$$

$$\frac{R_{\mathrm{tip}}}{R_{\mathrm{s}}} = \cos\varphi = \frac{L_{\mathrm{p}}}{R_{\mathrm{s}} W} \sin\theta_{\mathrm{t}} = \frac{1}{W\Delta} \sin\theta_{\mathrm{t}} \tag{15}$$

where $W = \omega\tau$ is an angular velocity in a dimensionless form. Squaring Eqs. (14) and $R_{\mathrm{s}} \sin\varphi = L_{\mathrm{p}} \sin(\theta_{\mathrm{t}}/2)$, and adding them yields

$$\Delta^2 = \sin^2\frac{\theta_{\mathrm{t}}}{2} + \frac{1}{W^2} \sin^2\theta_{\mathrm{t}} \tag{16}$$

Let $g = \sin^2(\theta_t/2)$; this puts a restriction to the value of ≤ 1 . We can express Eq. (15) through g as

$$\frac{R_{\text{tip}}}{R_s} = \frac{2}{W\Delta}\sqrt{g}\sqrt{1-g} \tag{17}$$

Eq. (16) becomes

$$\Delta^2 = g + \frac{4g(1-g)}{W^2} \tag{18}$$

Solving Eq. (18) for g, we obtain

$$g_{1,2} = \frac{1}{2}\left(1 + \frac{W^2}{4} \mp \sqrt{\left(1 + \frac{W^2}{4}\right)^2 - \Delta^2 W^2}\right) \tag{19}$$

where the sign in front of the square root for g_1 is minus (which is the only relevant solution when $\Delta < 1$ because of the condition $g \leq 1$), and g_2 assumes a plus sign. Both g_1 and g_2 are relevant solutions when $\Delta > 1$, but only for the restricted values of W.

$$0 \leq W \leq W_{max} = 2\left(\Delta - \sqrt{\Delta^2 - 1}\right) \tag{20}$$

which is clearly seen in Figure 3.7. From $g = \sin^2(\theta_t/2)$, we obtain $\theta_t = 2\arcsin\sqrt{g_{1,2}}$.

The solutions of Eq. (19) are separated by $\Delta = 1$, as plotted in Figure 3.7a ($R_{\mathrm{tip}}/R_{\mathrm{s}}\ vs. W$) and Figure 3.7b ($\theta_{\mathrm{t}}\ vs. W$), wherein the trend lines vary away from those of the boundary. One can prove that the equation for the bold solid line separating solutions at $\Delta = 1$ in Figure 3.7a is

$$\frac{R_{\mathrm{tip}}}{R_{\mathrm{s}}} = \sqrt{1 - \frac{W^2}{4}} \tag{21}$$

Additionally, as W increases, both $R_{\mathrm{tip}}/R_{\mathrm{s}}$ and θ_{t} approach a plateau, thereby suggesting that the steady-state helix angle becomes constant for a large value. A larger value for W (at a given response time) represents a faster rotation of the nanostage. Consequentially, both φ and θ_{t} increase (cf. Figure 3.7). The rise in φ shrinks the helix, thus diminishing its radius. Increasing θ_{t} shortens the helix lead, yielding a more compact structure (see Figure 3.8 for detail). We also observe that the helix angle is restricted to a specific range for $0 < \Delta < 1$. For example, θ_{t} ranges from 0 to about $100°$ at $\Delta = 1$. The helices shown here are left-handed, but we can also fabricate right-handed helices (without changing the direction of the stage rotation) using downward growth. Eq. (15) also offers a solution for such downward growth at a steady state, similar to the overhanging structure with a slanted angle of ca. $160°$ (cf. Figure 3.2). For a certain range of Δ, Figure 3.7b shows that the helix angle θ_{t} can overcome 90° with increasing W,

thus stimulating downward growth. Therefore, chirality can be assigned to right- or left-handedness according to the value of W. However, printing a right-handed helix may terminate the growth, especially for $\Delta > 1$, because the supply of the charged nanoparticles becomes inadequate. On one hand, a large W implies an insufficient supply of incoming aerosols for steady-state growth. On the other hand, a longer persistence length L_{p} is generally preferred in this 3D nanoprinting technique. When L_{p} becomes smaller than R_{s}, the field lines can lose focus, and thus, they seemingly terminate the structure growth.

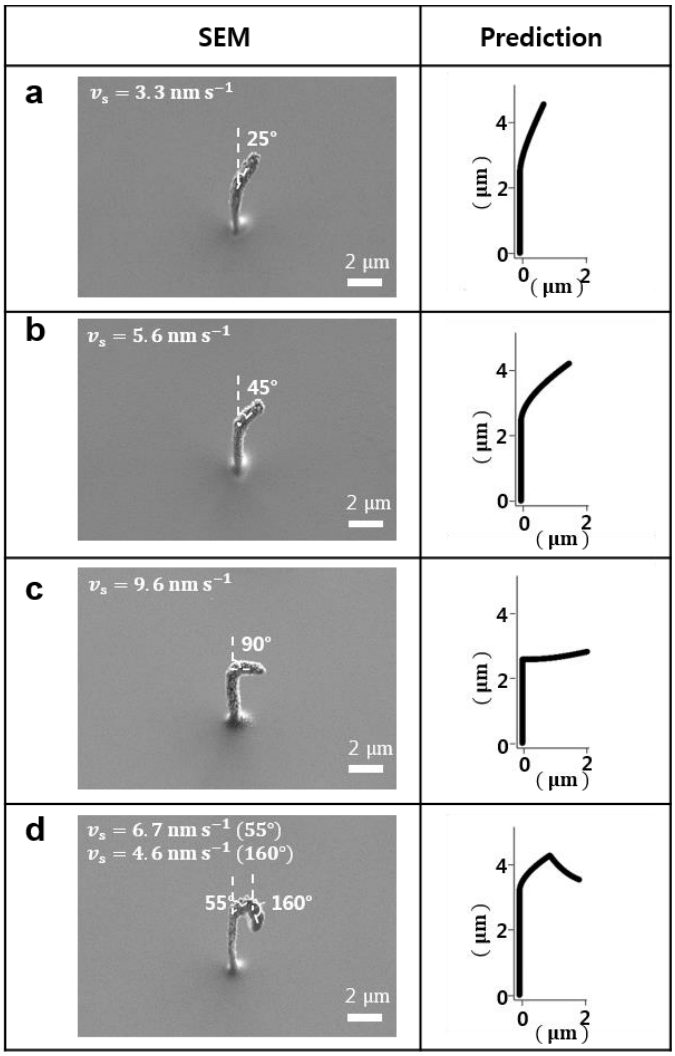

Figure 3.2. Comparison between experiment results of overhanging structure and phenomenological theory prediction. (**a**) 25° (**b**) 45° (**c**), 90° (**d**) 160°.

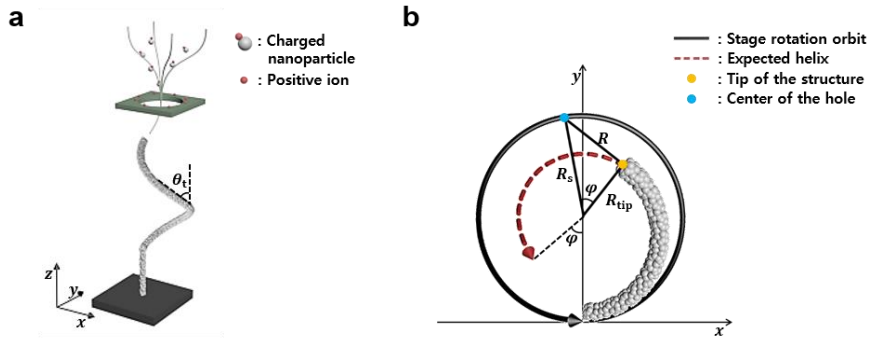

Figure 3.3. (a) The tilt view schematic of complete helix structure. **(b)** The projected schematic of the helix structure growth on the *xy* plane. The geometry corresponds to after the steady state. The red dashed line presents an expected helix after saturation, while the black line is the orbit of the nanostage. The green dot denotes the instantaneous tip, and the light-blue dot corresponds to the hole center on the mask. Helix structure has a constant R_{tip} and φ after the growth reaches the steady state.

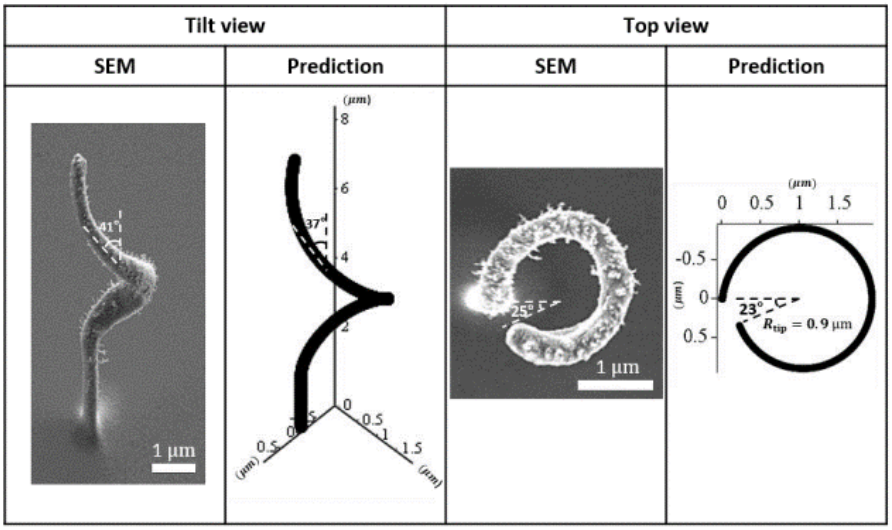

Figure 3.4. Tilt- and top-view of a single helix from 2.16b and the corresponding model predictions. The prediction model provides $R_{\mathrm{tip}} = 0.9\ \mu\mathrm{m}$, $\theta_{\mathrm{t}} = 37^{\circ}$, and $\varphi = 23^{\circ}$ whereas the SEM images of the experimental result show $R_{\mathrm{tip}} = 0.9\ \mu\mathrm{m}$, $\theta_{\mathrm{t}} = 41^{\circ}$, and $\varphi = 25^{\circ}$.

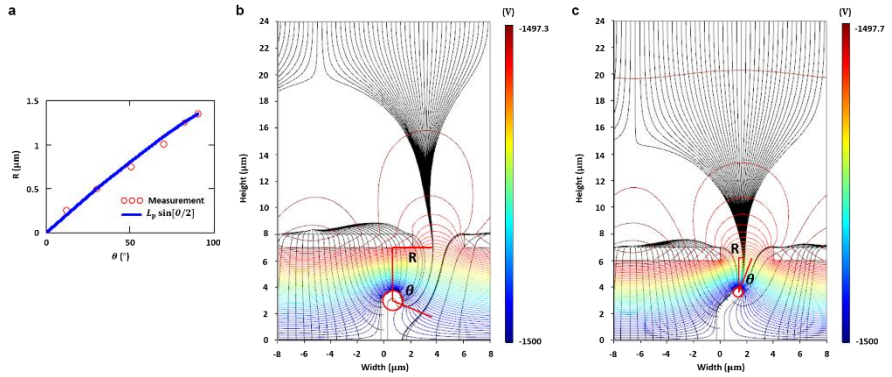

Figure 3.5. Electric field line calculations of the overhanging structures. (**a**) Comparison of calculation results with the phenomenological theory of R for various direction angles θ. The red circles are measured from calculation results for each slanted angle, and the blue line is calculated by Eq. (S2). L_{p} is about 1.9 μm when calculating R by Eq. (S2). (**b** and **c**) Calculation results of guiding line angle (**b**) $\theta = 113°$ and (**c**) $\theta = 21°$ cases. The guiding electric field line angle θ changes according to R. The red circle has the effective radius because the guiding field lines comes to the center of the red circle, not the tip. The surface charge density (σ) is $5.7 \times 10^{-6}\ \mathrm{C/m^2}$, the substrate voltage (including the structures) is $-1500\ \mathrm{V}$, and the upper boundary voltage is (**b**) $-1497.3\ \mathrm{V}$ and (**c**) -1497.7 V. Both side boundaries have a periodic condition.

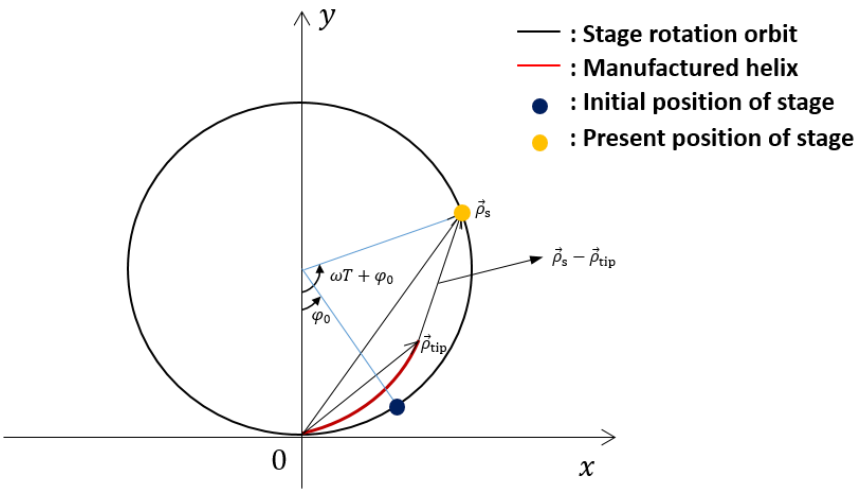

Figure 3.6. Explanation of the rotational motion configuration of the nanostage. The nanostage trajectory denoted by the black circle. At moment $T = 0$, it starts at φ_0 and rotates at angular frequency ω counterclockwise. The grown structure is shown in red.

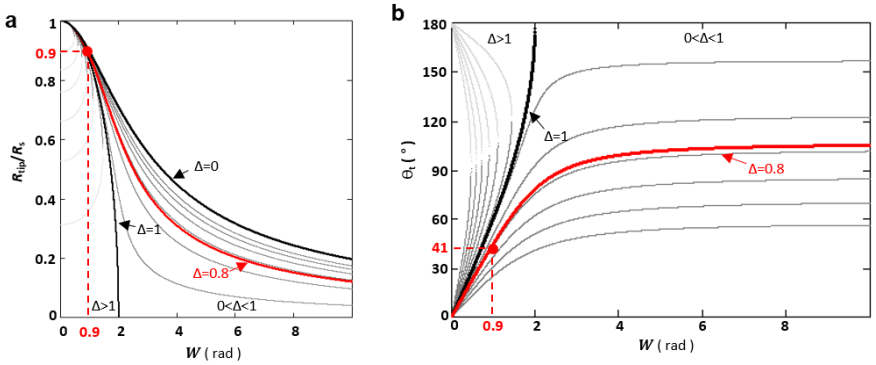

Figure 3.7. Prediction graphs of R_{tip}/R_s and θ_t $vs.W$ (**a**) Normalized helix radius as a function of a dimensionless angular velocity derived from Eq. (S13) for $0 < \Delta < 1$ and $\Delta > 1$. (**b**) Helix angle θ_t in relation to angular velocity W. The angle θ_t reaches a saturated value at different Δ. The lines, dots, and numbers in red represent the model predictions, corresponding to the SEM results in **Figure 2.20**. Light gray lines stand for the case of the second solution g_2 and meet the solution g_1 at the largest W_{max} after which growth is impossible. This non-growth lies in the range of $\Delta > 1$, whereas the helix growth always occurs for $0 < \Delta < 1$. For different Δ, the plateau represents the maximum helix angle.

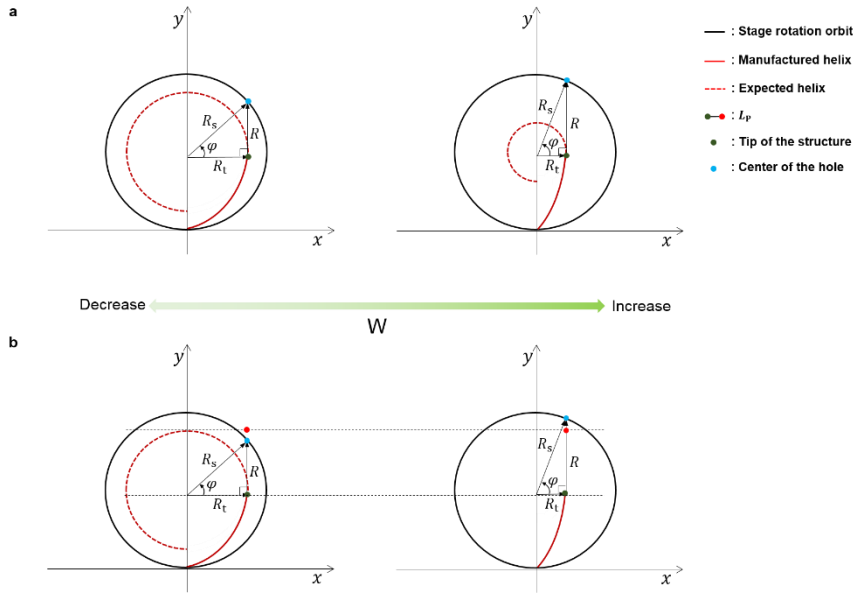

Figure 3.8. Explanation of the helix shape (**a**) Increasing the rotational speed of the nanostage (corresponding to a larger W) increases both φ and R, which diminishes the helix lead but increases the helix angle, leading to a more compact helix, as plotted in the right panel. (**b**) Interpretation of two W while maintaining the relation $R_s > L_p$. As presented in the left panel, we can make helices with a smaller W. When W increases further, R approaches the value of R_s, at which point the helix growth terminates.

3.4 Summary

In this work, we conducted theoretical analysis for metal 3D nanostructural growth. The well designed charged nanoparticle trajectory and phenomenological prediction model shows consistent results with experiment results.

In the nanoparticle trajectory simulation, we have explained nanostructure fabrication process from the behavior of nanoparticle. Nanoparticle trajectories are derived from solving the Langevin's equation. This simulation gives an angle of $27°$ for the overhanging structure in $25°$ and $44°$ for the overhanging structure in $45°$. This results explaining from the view point of building block proves that the shape of nanostructure can be controlled by mask moving along the electric field variation.

In addition, a phenomenological model has been developed for describing the 3D structure growth. The model predictions are remarkably consistent with the experimental results, therefore, provide a program for a complete control of our 3D nanoprinting. Thus, the new 3D nanoprinting for metal nanostructure array is expected to free the design process from restrictions imposed by other methods in terms of material choice, feature size, purity, and scalability.

Wooik Jung and Yoon-ho Jung equally contributed in this work.

3.5 References

[1] You, S., Choi, M. Numerical simulation of microscopic motion and deposition of nanoparticles via electrodynamic focusing. *J. Aerosol Sci.* **38**, 1140–1149 (2007).

[2] Hinds, W. C. *Aerosol technology: properties, behavior, and measurement of airborne particles*. (John Wiley & Sons, 1999).

[3] Visser, J. On Hamaker constants: A comparison between Hamaker constants and Lifshitz-van der Waals constants. *Adv. in Colloid Interface Sci.* **3**, 331–363 (1972).

[4] Israelachvili, J. N. *Intermolecular and surface forces*. (Academic press, 2015).

[5] Wangsness, R. K., Wangsness, R.K. *Electromagnetic fields*. (Wiley New York, 1979), vol. 2.

[6] Jones, T. B., Jones, T.B. *Electromechanics of particles*. (Cambridge University Press, 2005).

[7] Li, A. Ahmadi, G. Dispersion and deposition of spherical-particles from point sources in a turbulent channel flow. *Aerosol Sci. Tech.* **16**, 209–226 (1992).

[8] Khokhlov, A. R. *Statistical physics of macromolecules*. (Amer Inst of Physics, 1994).

Chapter 4. Concluding Remarks

In this dissertation, additive manufacturing of 3D metal nanostructure through electric field lines as a drawing tool was introduced. This technique is under fully dry condition and enables parallel nanoparticle assembly.

Firstly, we built 3D metal nanoprinting system based on previously developed ion assisted aerosol lithography. Owing to the nanoscopic lens effect which enables focused bunch of electric field lines, printed structures have nanoscale resolution even though opening site of floating mask has microscale diameter. In terms of feasible materials, the nanoparticle generation source has material flexibility in metals. We print multi-material structures consisting of Pd and Cu. We have also introduced that this 3D metal nanoprinting technique has two complementary modes: tip-directed growth and surface wrinting. Tip-directed growth manufactures vertical nanopillar, overhanging structures having diverse angles and helices, while surface writing shows rings and letters.

Second, the numerical analysis supports our strategy of 3D metal nanoprinting. The particle trajectory simulation explains behavior of charged aerosols so that the simulated nanoparticles accumulation shows consistent results to the experiment results in overhanging structure cases. In addition, a phenomenological model has been developed for describing the 3D structure growth. The model predictions are remarkably consistent with the experimental results, therefore, provide a program for a complete control of our 3D nanoprinting. Thus, the new 3D nanoprinting for metal nanostructure

array is expected to free the design process from restrictions imposed by other methods in terms of material choice, feature size, purity, and scalability. Concerning future applications, we envision further synergistic development with existing 3D printing technologies. We expect that the 3D nanoprinting method presented here will lead to a new paradigm in nanofabrication, in combination with currently successful 3D printing methods.

Acknowledgement

This work has been supported by the Global Frontier R&D Program of the Center for Multiscale Energy System (2012M3A6A7054855) by the National Research Foundation (NRF) under the Ministry of Science and ICT, Korea. Thank you for Kijun Bang for AFM measurement and Jicheng Feng for constructive discussion. Wooik Jung and Yoon-ho Jung equally contributed in this work. Wooik Jung, Yoon-ho Jung and Mansoo Choi planned the strategies for 3D nanoprinting; Wooik Jung and Yoon-ho Jung conducted experiments; Peter V. Pikhitsa built the phenomenological model; Wooik Jung, Yoon-ho Jung, Jooyeon shin and Mansoo Choi analyzed data and designed figures. In addition, the research of this thesis will be published in the academic journals.

하전된 에어로졸을 이용한 삼차원 금속 나노구조물 어레이의 적층 제조

서울대학교 대학원 기계항공공학부

정 우 익

요약

삼차원 (3D) 프린팅으로 알려진 적층 가공은 형상에 구애받지 않고 적은 비용으로 넓은 면적에 신속한 프린팅하는 것을 목표로 한다. 특히, 3D 프린팅 된 금속 나노 구조물은 다양한 분야에서 광범위한 수요가 존재하나 3D 나노프린팅 기술 연구는 대부분 고분자 물질에 집중되어 있어 금속 3D 나노프린팅 기술은 나노스케일 해상도, 빠른 속도, 고순도 및 복잡한 형상을 동시에 달성하지 못했다. 이러한 문제점들을 해결하고자 우리는 대기압에서 병렬 방식의 금속 3D 나노 구조물 제작이 가능한 에어로졸 3D 나노프린팅 기술을 개발했다. 부유형 마스크 표면에 축적된 이온들에 의해 왜곡된 형상의 전기장에 직교하는 전기력선들을 따라 하전된 금속 나노입자들은 나노스테이지 위에 부착된 기판에 축적되고, 자유로운 3D 금속 나노프린팅을 가능하게 했다. 이 기술은 나노스테이지의 이동 속도에 따라 두가지 모드로 구분될 수 있다. 상대적으로 나노스테이지의 움직임이 느린 “팁 지향적 모드”에서는

수직 및 기울기를 가진 나노스케일의 기둥과 나선 형상을 인쇄할 수 있고 이와 반대로 나노스테이지의 움직임이 빠른 “쓰기 모드”에서는 기판에 나노스케일로 원하는 형상을 쓸 수가 있었다. 이 공정은 대기압 상에서 이루어지며 액상 등의 고분자 물질이 필요하지 않기 때문에 높은 순도의 금속 나노구조물을 제작할 수 있으며 사용 가능한 금속의 제한이 없으며, 프린팅된 구조물의 강화를 통해 높은 전기 전도도와 기계적 강도를 가질 수 있다. 또한, 이론적 분석 모델을 통해 3D 구조물의 형상을 예측할 수 있는 모델을 개발했으며 실험적 결과와 일치하는 것을 확인해 사용자 친화적인 삼차원 나노프린팅 기술로 발전할 수 있음을 보였다. 우리는 이 기술이 3D 나노프린팅 연구 분야에 새로운 패러다임을 가져와 여러 분야에 적용되는 초석이 될 수 있기를 기대한다.

주요어: 금속 3D 나노프린팅, 전기력선, 에어로졸, 고순도, 병렬 방식, 팁 지향적 모드, 쓰기 모드

학번: 2013-23836